

THE HAGUE UNIVERSITY OF APPLIED SCIENCES
ENGINEERING PHYSICS

On developing a detector for a muon tomography system



AUTHOR: Ian T. Huizenga (20122489)
SUPERVISOR (NIKHEF): Dr. M. Fransen
EXAMINER (THUAS): Mr. H. Snijder
COORDINATOR (THUAS): Ms. C. Van Tour
DATE: 4/7/2024

Abstract

This paper researches and discusses a novel method for a muon tomography system with the main focus being on researching how aspects of detector geometry, such as depth, surface area, and sensor amount affects its positional resolution.

For this, a python model was constructed that simulates the core physics at hand. With this, an equation governing the light measured N by a detector as a function of distance R to a cosmic ray hit in a scintillator was found, namely;

$$\langle N \rangle = N_0 (\cos \theta_c) \left(1 + \frac{2R}{X_0} - \frac{2R}{X_0 \sin \theta_c} \right) \left(\frac{1}{\pi} \arctan \frac{L}{2R} \frac{\vec{\mu} \cdot \vec{n}}{|\mu||n|} \right)$$

This equation could then be used to fit the light measured by several Silicon photomultipliers to obtain a reconstructed position of where the cosmic ray had hit the detector. Due to statistical fluctuations in light measured, this fitting procedure has some uncertainty. This uncertainty, expressed as the standard deviation, is dependent on certain aspects of detector geometry.

It was found that for the proposed detector, a square scintillator with sensors on each lateral face, a positional resolution ranging from 3-6 mm was fairly easy to achieve without an unreasonable scintillator geometry or amount of sensors.

Using these results, a simple muon detector was constructed that allowed for real-time observation of cosmic rays bombarding the detector. Unfortunately, the expected uncertainty and the measured uncertainty differed by a factor 2. This can be explained by the Cosmic Watches used to analyse the signal before being processed. These were never designed to be used for precise measurements, and therefore have quite a substantial effect on the position resolution.

Lastly, it was found that placing sensors at the sides of a scintillator yields undesirable "blind spots" that drastically reduce the accuracy. To solve this in the future, it is recommended to place the sensors at the corners of the scintillator.

With this, the groundwork has been laid for a fully functioning muograph with a positional resolution that is sufficient for practical use.

Contents

1	Introduction	3
2	Theory	5
2.1	The principles of muon tomography	5
2.2	Cosmic rays & muons	6
2.3	Energy loss in materials	8
2.3.1	Excitation & Ionisation	8
2.3.2	Scattering	11
2.4	Photon traversal through scintillator	13
3	Setup	19
3.1	Scintillator	19
3.2	Silicon photomultiplier	20
3.3	Measurement setup	22
4	Model	24
4.1	Modelling the theory	24
4.2	Expected result	26
4.3	Position determining	26
5	Results	30
5.1	Verifying the model	30
5.1.1	The position determining algorithm	34
5.2	Dependency of spatial resolution on detector geometry .	36
5.3	Creation of a muon detector	38
6	Discussion & Recommendations	46
7	Conclusion	47
8	Acknowledgements	48
9	Literature	49
10	Appendices	51

1 | Introduction

Back in 2011, the East Coast of Japan was hit by a tsunami, a calamity which significantly damaged the Fukushima Daiichi Nuclear Power Plant, causing severe environmental harm. Due to the high radiation level, it was difficult for the damage analysis of the reactor to be provided. In the end, despite the many procedures that were used, such as X-Rays and Gamma Ray Imaging, no devices could be set up nearby the reactor core. Therefore, a different technique was needed, in order to visually represent the core of the reactor, namely Muon tomography. [1].

Muon tomography involves muons, subatomic particles generated by cosmic rays, which traverse through dense matter and impart some, if not all of their energy into said matter. Due to this, it is possible to get a density scan of a material based on the amount of muons reaching the detector, through a process similar to an X-ray. Its benefits lie in the abundance of cosmic rays (1 muon per cm^2/min), as well as the fact that it doesn't require as much preparation when compared to a radiographic detector. It also proves as advantageous because cosmic muons have such a high velocity that they can traverse hundreds of meters before they decay. The scanning of large, spent nuclear fuel tanks should be of interest, as it often contains highly radioactive, dense materials, such as uranium. In order to accurately obtain a density scan for these tanks, a detector with an accuracy of a few millimetres is required. The detector used in the aforementioned Fukushima incident had an angular resolution of 4mrad [1], which translates to a positional resolution of 4mm, with two detectors placed a metre apart. This accuracy is highly dependent on detector size and depth, amount of sensors and type of components used, all of which will be later on discussed in this paper.

Starting with the 21st century, the advent of many technological innovations has greatly impacted the semiconductor industry: Components became increasingly smaller, dropping to the size of mere atoms, this rapid development also resulted in substantial computational advancements. In comparison to a decade ago, compact sensors are now at a significantly lower production cost, therefore allowing for a broader range of usage. The present paper will analyse the ways in which modern advancements can be used to create a cheaper, more compact version of a muon tomograph, a detector that allows for 2D, possibly even 3D scans of large objects, in the areas where X-ray imaging would be impractical or undesirable.

The question that is central in this research paper is as follows: "How does the position resolution depend on detector geometry and is it feasible to build a system that has a performance sufficient for practical use? (order of a millimetre)" In order to do so the key points to research will include, but are not limited to: both sensor size and amount, overall size of the detector and the configuration of the sensors, meaning where they are placed on the detector.

This shall be approached by constructing a simulation of the entire process, starting with a cosmic muon hitting the detector and finishing with its impact position being determined. While the simulation is ongoing, each step shall be accounted for, checked and later on confirmed by data, either provided by reliable sources or obtained through measurements. After the model is thoroughly validated, the different parameters previously named can be adjusted, in order to optimise the spatial resolution, while minimising factors such as the amount of sensors used and the size of the detector.

For the creation of the model to be possible, it is important to firstly understand the core physics which allow for muon tomography to work. These aspects will be examined in the following section.

List of commonly used variables

Symbol	Definition	Units or Value
$\langle \frac{dE}{dX} \rangle$	Mean particle energy loss	MeV/g/cm ⁻²
E	Particle kinetic energy	MeV or GeV
β	Relativistic factor v/c	(-)
γ	Lorentz factor $\frac{1}{\sqrt{1-\beta^2}}$	(-)
c	Speed of light	299 792 458 m/s
p	Particle momentum	MeV/c or GeV/c
m	Particle mass	MeV/c ²
$m_e c^2$	Electron mass $\times c^2$	0.510 998 918 MeV
N_a	Avogadro's constant	6.022 1415 $\times 10^{23}$ mol ⁻¹
r_e	Electron radius	2.817 940 325 $\times 10^{-15}$ m
Z	(Mean) Atomic number of scintillator	(-)
A	(Mean) Atomic mass of scintillator	g/mol
K/A	$4\pi N_a r_e^2 m_e c^2 / A$	0.307 075 MeV/g/cm ⁻²
Q_{max}	Maximum transferable kinetic energy to electron	MeV
I	Mean excitation energy	MeV
X_0	Radiation length	g/cm ²
δ	Density effect parameter	(-)
ρ	Scintillator density	g/cm ³
L	Distance travelled in scintillator	cm
L_0	Light attenuation length	cm
N_0	Amount of photons created during scintillation	(-)
N	Amount of photons measured by sensor	(-)

all data is sourced from [2]

2 | Theory

This section gives an overview of all the relevant processes to muon tomography. Everything from the creation of muons in the upper atmosphere and how they interact with matter through to what SiPM's are and how they can be utilised in muon tomography. However, it is first important to explain what muon tomography is.

2.1 | The principles of muon tomography

Muon tomography [3], or muography is in principle very similar to regular tomography (used in a CT scan) in the sense that a particle travelling through a material will get absorbed more rapidly if said material is denser. With this, an absorption profile can be made of any object that is suitable [4]. However the downside with CT scans is that it requires X-rays something that does not naturally occur and has to be generated. For instance, one cannot easily use a CT scan on a building to observe weaknesses in the reinforcement of concrete pillars. This is where muography comes in; muography works on a similar basis, where muons, generated in cosmic rays (see section 2.2), get scattered, and/or absorbed by denser materials [2]. Allowing for a density scan of objects as large as a volcano [5]. In fig. 1 a sketch can be seen on how cosmic rays create muons, which then traverse through matter, where denser objects have a higher stopping power (section 2.3) and thus are able to absorb some - or all - of the muon's energy.

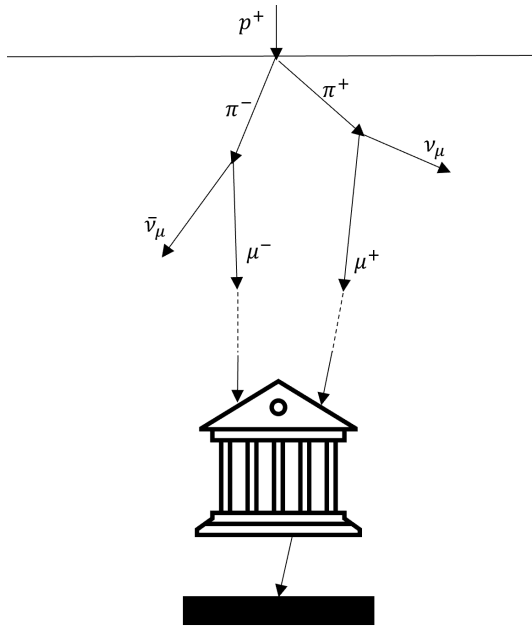


Figure 1: An example of how muography works. Muons (μ^-) and antimuons (μ^+) get created, where a fraction of the muons get absorbed in denser materials.

As can be seen, this is an accurate, non-invasive technique using a readily available muon flux (approximately, one per minute per square centimetre [6]. Or, in other words, if one held out their hand, one muon would pass through each second). For these reasons, it is clear why muography could see extensive use in a large array of fields. Everything from observing spent nuclear fuel tanks to analysing volcanoes and seeing what areas have potentially dangerous lava flows close to the surface.

2.2 | Cosmic rays & muons

Now that the basics of tomography are explained, it is important to elaborate on what muons are and how they get created.

Muons are one of the elementary particles in the standard model of particle physics (see fig. 2). They are a second generation particle, having a similar charge but a greater mass than their first generation counterpart, the electron [7].

Standard Model of Elementary Particles

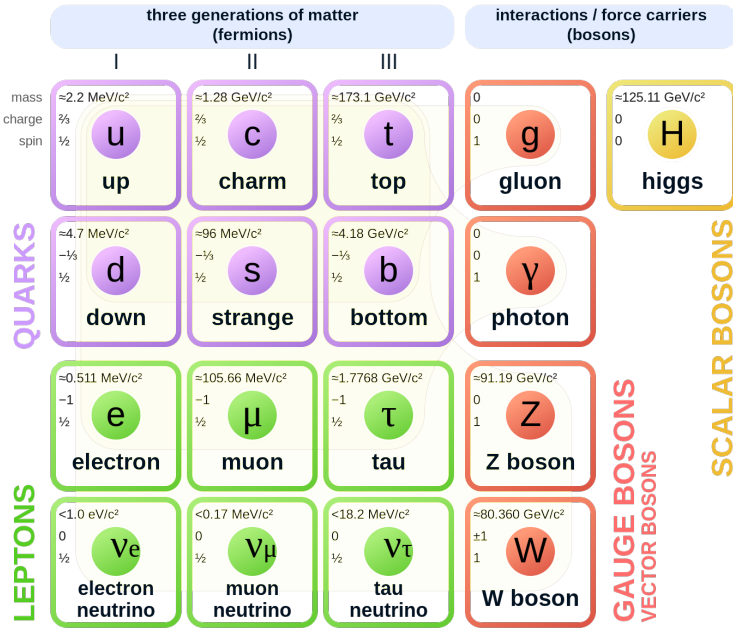


Figure 2: The standard model of particle physics showing each fundamental particle from every generation, as well as their interaction particles. This theory encompasses three of the four fundamental forces; electromagnetism, the weak nuclear and strong nuclear force and is largely considered to be one of the most successful theories in physics [8] [9].

Their mass is approximately 207 times heavier than that of an electron, this being $106 \text{ MeV}/c^2$ (compared to an electron's $0.511 \text{ MeV}/c^2$). Due to this heavier mass, they are much less likely to get scattered (section 2.3) in a material, and thus have a higher penetrative depth compared to electrons. Most muons measured on earth are created in the upper atmosphere during a violent collision with a cosmic ray [10]. Most cosmic rays ($\sim 90\%$) are protons; a smaller percentage are electrons; anything heavier than helium is exceedingly rare.

When a (primary) cosmic ray collides with the upper atmosphere, a large amount of exotic secondary particles are created. These can include photons, various mesons (composite particles with a quark-antiquark pair), and neutrinos [11]. Pions are one type of particle that can be created; they are formed by combining an (anti) up quark with an (anti) down quark. These have a relatively short lifetime and depending on the type of pion, they decay in, at most, 26 nanoseconds. They then decay into a muon and a muon neutrino.

The way this decay can be represented is using what is known as a Feynman diagram. These diagrams are representations of complicated underlying mathematics and serve as a useful visual aid in understanding the subatomic interactions. In figure 3 a Feynman diagram is shown of a pion decaying into a muon.

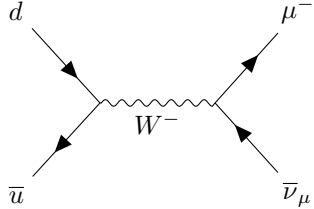


Figure 3: Feynman diagram of a negatively charged pion (anti up and a down quark) decaying into a muon and anti-muon neutrino. This process occurs in approximately 26 nanoseconds after the primary cosmic ray impact. Time flows from left to right in this diagram [12].

After this, the muon that gets created traverses the atmosphere at velocities close to the speed of light. At the time of creation, the average muon will have a kinetic energy of 6 GeV, this equates to a velocity of 0.99985% the speed of light [7]. Due to this high velocity, special relativity has to be taken into account (specifically time dilation and length contraction) to explain how they can be measured on earth [13].

A muon's lifetime is approximately 2.2 microseconds. Using classical mechanics this implies they could never traverse the entire atmosphere since they would decay before ever reaching the surface. However due to their extremely relativistic velocities, from the perspective of an observer, they undergo heavy time dilation, to the point where that 2.2 microseconds gets dilated all the way to 86 microseconds. Which is plenty of time for the muon to reach the earths' surface. After those 2.2 microseconds a muon decays into an electron, anti electron neutrino, and a muon neutrino [7]. This can be seen in fig. 4. Due to the large mass difference in the muon and electron, and to conserve momentum. The resulting electron has a much greater velocity than the decaying muon.

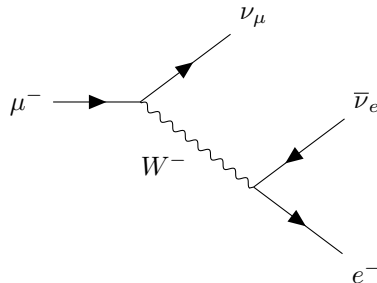


Figure 4: Feynman diagram of a muon (μ^-) decaying into an electron (e^-), anti electron neutrino ($\bar{\nu}_e$), and a muon neutrino (ν_μ).

As stated before, muons have on average 6 GeV of kinetic energy upon creation. However, as they traverse through the atmosphere, interactions with atoms and molecules reduce some of their initial energy, losing about 2 GeV of energy, with a kinetic energy of 4 GeV at sea level. One can imagine that a material with more atoms (higher density) attenuates the muons kinetic energy more than a material with less atoms. These interactions and how muons lose their energy will be explained in the next section.

2.3 | Energy loss in materials

There are different effects that can occur when particles such as muons go through matter, for the sake of clarity, only those relevant to muon tomography are discussed here.

2.3.1 | Excitation & Ionisation

Excitation takes place when a particle transfers some of its kinetic energy to an electron in an atomic structure. In this paper, a scintillator is being studied, a special type of material that facilitates easier excitation and ionisation (see section 3.1). This energy transfer is equal to one of the energy levels of an electron. This ‘excited state’ is unstable and will quickly fall back down to its original energy level, releasing a photon in the process [14]. This can be seen in fig. 5.

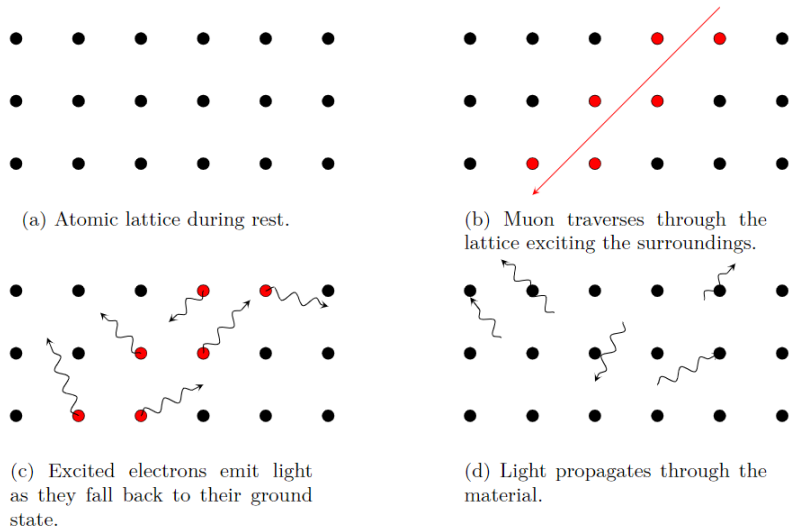


Figure 5: Simplified graphic showing how a muon excites the surrounding atoms. It is important to note that although the figure displays an atomic lattice, similar to a crystal structure. This can happen to any material regardless of whether it is in a crystalline state.

The mean energy that the muon imparts into the electrons can be derived semi-classically and results in the Bethe-Bloch equation [2]:

$$-\left\langle \frac{dE}{dx} \right\rangle = K \frac{Z}{A} \frac{1}{\beta^2} \left[\frac{1}{2} \ln \frac{2m_e c^2 \beta^2 \gamma^2 Q_{max}}{I^2} - \beta^2 - \frac{\delta}{2} + \frac{1}{8} \frac{Q_{max}^2}{(\gamma m c^2)^2} \right] \quad (1)$$

The most important terms within the brackets are the first and second term. These account for most of the effects visible in the energy spectrum cosmic muons are most prevalent (low GeV’s). The other terms are minor corrections at lower and higher energies. One more term for ” breaking radiation” or bremsstrahlung, is only visible at extremely high energies (high GeV’s/low TeV’s) and is therefore not shown. In figure 6 the Bethe-Bloch equation is plotted.

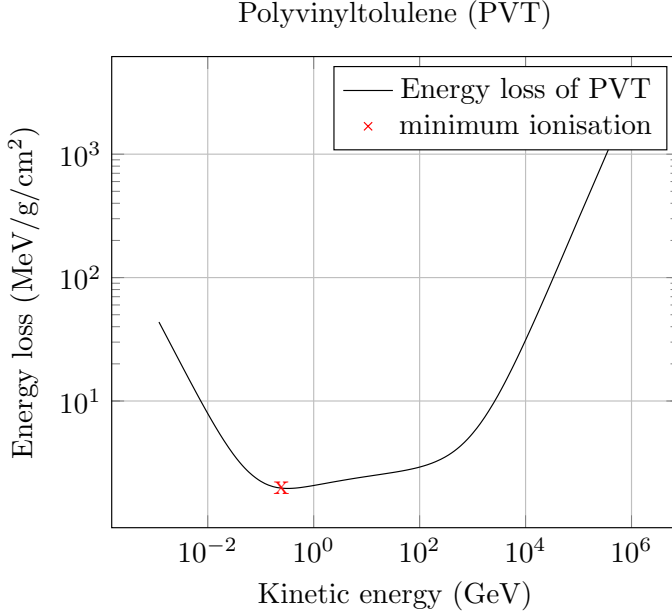


Figure 6: Full Bethe-Bloch equation for polyvinyltoluene (PVT), a common plastic scintillator. From 10 MeV all the way to 1000 TeV, including bremsstrahlung [15].

The initial decrease in energy loss as velocity increases is due to the $1/\beta^2$ term in eq. 1, After it reaches its lowest point (minimum ionisation), it slowly starts to increase again, in what's called a relativistic rise. This happens due to the $\beta^2\gamma^2Q_{max}$ term inside the brackets of eq. 1. After this, the strong rise occurs due to the aforementioned bremsstrahlung.

As can be seen, the average energy loss of cosmic muons lies in the range of 1-3 MeV/g/cm⁻². However, energy loss is a stochastic process and will therefore fluctuate around this mean. The nature of which will be explained in the following section.

The Landau distribution

As stated before, the energy loss resulting from the Bethe-Bloch equation is merely an average and not the total energy loss. The proper energy loss is a statistical process which follows an uneven distribution named the Landau distribution [16]. This distribution has a sharp peak and a long and "fat" tail. Due to this, parameters such as variance and mean are generally not known (with the exception of the mean being known in this specific circumstance). in fig. 7, the Landau distribution for the point of minimum ionisation can be found. The Landau distribution is generally characterised by two parameters, μ and σ . μ is the location parameter, which governs where the peak (or most probable value) of the landau is found. In this case one can use the average found in the Bethe-Bloch. This does not mean that μ is the most probable value (MPV), it is simply a parameter to characterise it. σ gives an indication of the width of the landau and it is typically characterised as follows [2]:

$$\sigma = 2K \frac{Z}{A} \frac{1}{\beta^2} \quad (2)$$

This is simply twice the first term in the Bethe-Bloch equation.

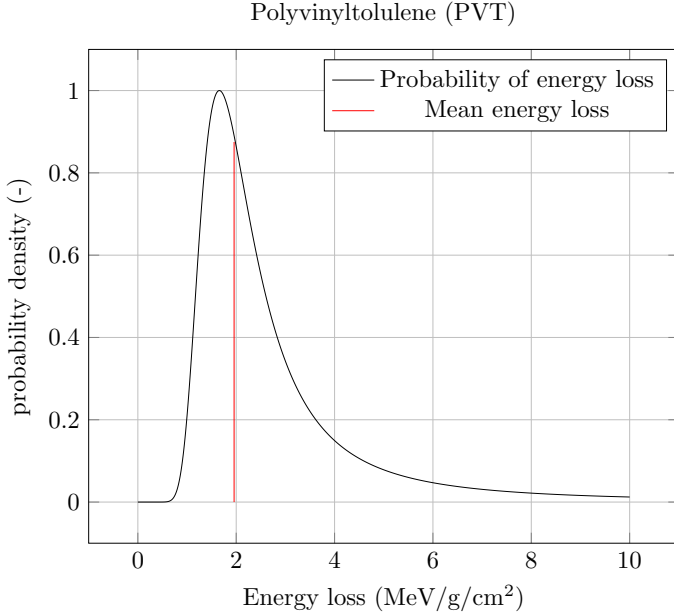


Figure 7: Normalised Landau distribution for a muon traversing through PVT. This is the energy loss belonging to the kinetic energy at minimum ionisation seen in fig. 6.

Of course, this still does not give the proper amount of energy lost. After all MeV/g/cm⁻² are not units of energy, they are simply "normalised" values of energy loss, not accounting for both depth as well as density. To see how much energy is lost per centimetre of material one needs to multiply the energy loss with the density to find how many MeV/cm is lost. After this, multiplying with the depth traversed finds how many MeV are deposited into the material. Most of this energy eventually gets converted into light. However, at higher energy losses this becomes slightly nonlinear [17]. This will be described in the following section.

Nonlinearities in photon generation

To convert the amount of energy lost into the amount of photons, one could simply multiply the energy loss with a certain "gain", this gain S , is how many photons per MeV of material are generated, this is a material specific constant. For PVT, and most other plastic scintillators it is approximately 10 000 photons per MeV.

At low energy losses, this relation is linear. One MeV will produce 10 000 photons, two produces 20 000. However, due to an effect called "quenching" where excited electrons recombine with vacant holes, occurring at higher energy losses. Six MeV won't produce 60 000 photons and is actually closer to 50 000. The equation that governs this nonlinearity is called Birks' law [17]:

$$\frac{dL}{dx} = S \frac{dE/dx}{1 + k_b dE/dx} \quad (3)$$

Where dL/dx is the amount of photons L over a distance x , S is the aforementioned gain, and k_b is Birks' constant, a variable that is material specific and governs how nonlinear the photon yield is. As can be seen. At low energy losses, the denominator tends to 1, and thus the linear correlation one would expect can be seen. However, at higher energy losses it gradually becomes less linear.

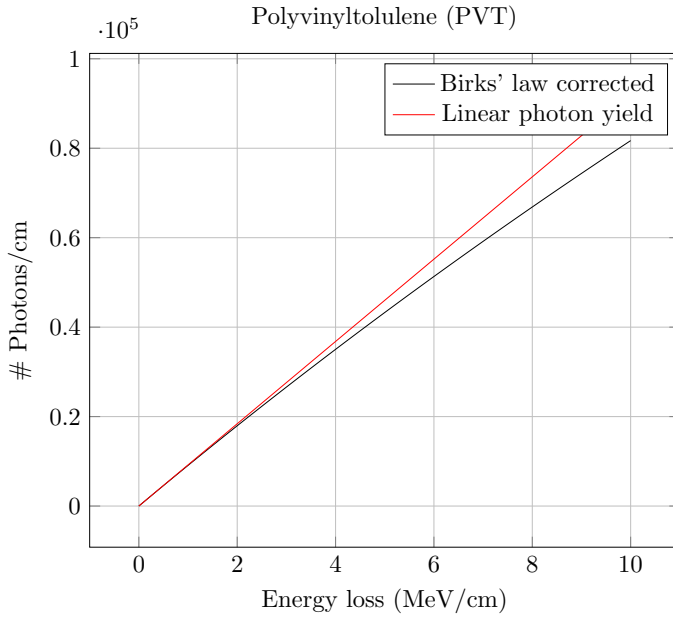


Figure 8: Nonlinear energy losses for a minimum ionising particle (MIP) in PVT. $S = 9200 \text{ MeV}^{-1}$ and $k_b = 0.0126 \text{ cm/MeV}$

Of course, at the low energy losses with cosmic muons and low Z scintillators, this effect won't have much of a role. However for the sake of accuracy it shall be included regardless.

However, the ionisation track is not actually a straight line, as is shown in fig. 5. Once a negatively charged muon comes close to a negatively charged electron, it will get repelled. This effect is known as scattering and will be discussed in the following section.

2.3.2 | Scattering

Scattering occurs when an incident particle, in this case a muon, gets deviated from its original trajectory when it undergoes electrostatic repulsion [18]. The main form of scattering of interest for muography is Coulomb scattering. This is where a charged particle undergoes electromagnetic repulsion due to the electrons around an atom (see fig. 9). This then causes the particle angle to deviate from its incident angle.

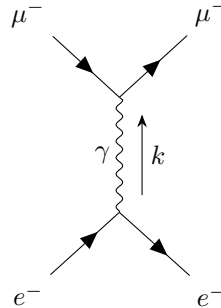


Figure 9: feynman diagram of a muon coming close to an electron and undergoing electromagnetic repulsion, via a momentum transferring photon (k), which causes scattering.

This, of course, can happen many times in a material. The result is that there is a statistical deviation between the incident and emergent angles. This can be approximated as a Gaussian curve (fig. 10).

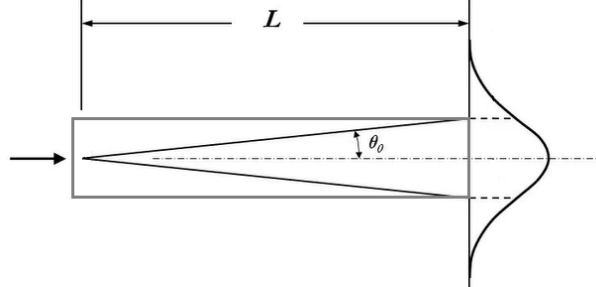


Figure 10: Diagram of multiple scattering

The standard deviation of this Gaussian, X_0 , is related to the scattering angle θ_0 , which is given by the Moliere equation seen in eq. 4 [19].

$$\theta_0 = \frac{13.6 \text{ MeV}}{\beta cp} \sqrt{\frac{L}{X_0}} \left[1 + 0.038 \ln \left(\frac{L}{X_0} \right) \right] \quad (4)$$

Here, p is the momentum of the incident particle. The radiation length X_0 is the mean length where the energy of an incident particle is reduced by e^{-1} . One can assume that this length is dependent on both density (ρ) and atomic number (Z). So for denser materials such as uranium or steel the radiation length is much shorter, which in turn leads to a large scattering angle. This can also be seen in eq. 5.

$$X_0 = \frac{716.4 \text{ g} \cdot \text{cm}^{-2} \text{A}}{\rho Z (Z + 1) \ln (287/\sqrt{Z})} \quad (5)$$

This strong dependence on both Z and ρ is what makes muon tomography suitable for imaging denser materials [19].

Now that it is known how much light gets generated during scintillation, it is important to look at how this light traverses the material to finally end up at a detector.

2.4 | Photon traversal through scintillator

When a muon traverses through a scintillator it produces a track of photons (see fig. 5), which move outward in, approximately, a cylinder shape. To find how this propagation of light traverses through the material, and to get an analytical solution, an assumption has to be made, namely;

All light generated during scintillation is created in a point source in the centre of the scintillator. (see fig. 11.)

This is accurate when the scintillator is thin compared to its length, a material is considered "thin" if the distance R to a detector is more than twice the thickness L :

$$2L < R \quad (6)$$

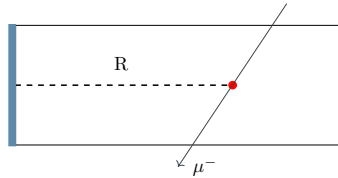


Figure 11: Side view of a scintillator. At some distance R away from a detector (marked blue in figure), a point source of light (red dot in figure) is created as a muon traverses through a scintillator.

Now that this assumption is made, an analytical solution can be found. Firstly, the point source has an initial amount of photons generated over the entire track length. This can be called N_0 . Of course, one can understand that the photons detected at the sensor will be proportional to the amount of photons created.

$$N \propto N_0 \quad (7)$$

After this, the light will propagate spherically outward until it reaches the upper and lower boundary where it will, depending on the angle, either reflect internally, or have a probability to do so. This probability is governed through the Fresnel equation, which is displayed in fig. 12.

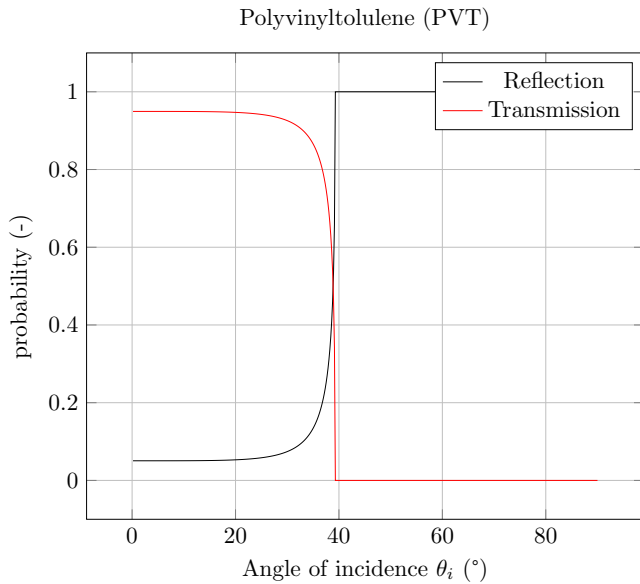


Figure 12: Plot of the reflection and transmission coefficients of PVT and air.

As can be seen. Any photons reaching the top and bottom below the critical angle have a probability to be reflected, anything greater than the critical angle θ_c will stay inside of the scintillator. Considering an analytical solution is impossible when using probabilities, another assumption has to be made;

All light within the critical angle gets transmitted and none gets reflected. (see fig. 13)

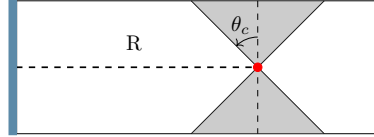


Figure 13: Side view of a scintillator. All light within the "cone" is not internally reflected and therefore will be lost.

Of course. This is only valid for distances that are outside of this cone. For this, three separate "ranges" are determined. A close, mid and far range. The far range is defined the same as eq. 6. The midrange is defined as $L \leq R \leq 2L$, and close range is anything smaller than L . For the sake of simplicity. The above approximation is only valid for far range, and will produce errors in mid and close range.

To find out what fraction of light gets internally reflected, one needs to find the solid angle of the cone made by the critical angle θ_c and find out what the fraction of the solid angle is without this cone. Since the solid angle of a cone is: $\Omega = 2\pi(1 - \cos \theta_c)$ and since there are two cones, both on the top and bottom one can write the following:

$$N \propto N_0 \left(\frac{4\pi - 2\Omega}{4\pi} \right) = N_0 \left(\frac{4\pi - 4\pi(1 - \cos \theta_c)}{4\pi} \right) \quad (8)$$

which, when simplified, yields the following expression:

$$N \propto N_0 (\cos \theta_c) \quad (9)$$

Clearly, as the critical angle gets smaller, more light will get internally reflected and thus less will be lost.

As this light travels through the material (see fig. 14) it will travel a longer distance than simply R .

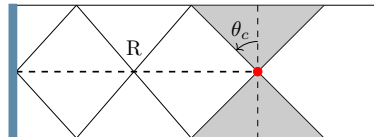


Figure 14: Side view of a scintillator. Light that is internally reflected will propagate through the material

Therefore, At longer distances, due to light scattering and absorption, there is an increasing probability that internally reflected light will get attenuated and will thus never reach the detector. This exponential decay is formulated with the Beer-Lambert law [20]:

$$N \propto N_0 e^{-\mu d} \quad (10)$$

Where μ is an attenuation coefficient, often written as $1/X_0$ and d the distance travelled by the light. Of course, this is only for a single photon traversing a specific distance d which is simply and considering it will be challenging to find an analytical solution for a larger quantity of photons, this equation needs

to be simplified. This can be done by taking the first-order Taylor expansion of the function and thus linearising it. This results in the following:

$$N \approx N_0 \left(1 - \frac{d}{X_0} \right) \quad (11)$$

Now, considering that d is the specific distance travelled by a single photon one can see that it is therefore also dependent on the angle at which the photon propagates, some trigonometry will show that: $d = R/\cos \gamma$, where γ is the specific angle each photon path has with respect to the horizontal, with its maximum belonging to the complementary angle of θ_c , I.E $\gamma_{max} = 90 - \theta_c$. Considering the interest lies in finding a function governing the general attenuation of photons over a range of angles. It is worth finding the rate of change in photons measured depending on the incident angle. In other words, differentiate, with respect to γ .

$$\frac{dN}{d\gamma} \propto \frac{d}{d\gamma} \left(N_0 - \frac{N_0 R}{X_0 \cos \gamma} \right) = -\frac{N_0 R \tan \gamma}{X_0 \cos \gamma} \quad (12)$$

As expected, the sign in front of the function is negative, implying that as γ increases, N decreases.

To find the total amount of photons that land on the detector there is one small trick that needs to be done. Finding how many photons per degree is tricky considering the light keeps reflecting and reaching the detector at different angles. For this reason, one can imagine that (since the angle of incidence equals the angle of reflection) no reflection occurs at all and the photon simply traverses the material at angle γ until it reaches the edge at distance R . Due to this, the outermost photon paths (the paths that are on the edge of being internally reflected) in fig. 14, can be unfolded to form a triangle, or cone. which still has each photon travel the same distance, but without any reflections (see fig. 15). It is important to note that this does not mean the photons exit the scintillator, it is merely a tool to simplify the mathematics.

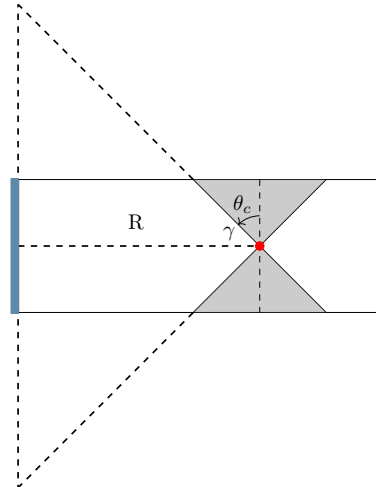


Figure 15: Side view of a scintillator. The reflections from fig. 14 can be unfolded to reveal a simpler, easier to work with shape. The path travelled for each photon stays the same.

In appendix A. A picture of a scintillator can be seen from the "perspective" of a light source propagating through a material. This aids in visualising the concept of "enlarging" the detection area.

Now that the shape has been simplified, it is easy to see that the maximum angle γ is simply the complement of θ_c . To now get the total amount of photons hitting the side of the detector (entire vertical dotted line in 15). The rate of change can simply be integrated along the entire axis from $+\gamma_{max}$ to $-\gamma_{max}$. This then results in,

$$\int_{N_0}^N dN \propto -\frac{N_0 R}{X_0} \int_{-\gamma}^{+\gamma} \frac{\tan \gamma}{\cos \gamma} d\gamma \quad (13)$$

Here, dN is integrated from N_0 , the amount of photons at the point source, to N , the amount of photons at the location of the sensor.

Of course, since the function is vertically symmetric, this is the same as integrating one half, twice.

$$N - N_0 \propto -\frac{2N_0 R}{X_0} \int_0^\gamma \frac{\tan \gamma}{\cos \gamma} d\gamma = -\frac{2N_0 R}{X_0} \left[\frac{1}{\cos \gamma} \right]_0^\gamma = -\frac{2N_0 R}{X_0} \left[\frac{1}{\cos \gamma} - 1 \right] \quad (14)$$

After a little rearranging the following equation appears:

$$N \propto N_0 \left(1 + \frac{2R}{X_0} - \frac{2R}{X_0 \cos \gamma} \right) \quad (15)$$

After noting that $\gamma = 90^\circ - \theta_c$ and combining it with eq. 8:

$$N \propto N_0 (\cos \theta_c) \left(1 + \frac{2R}{X_0} - \frac{2R}{X_0 \sin \theta_c} \right) \quad (16)$$

This is not the full picture however. This equation does account for all photons internally reflected and for scattering and absorption attenuation. However, a big part that is missing considers the sensor size. One can imagine that a larger sensor, catches more photons.

To simplify the situation, and by making use of earlier made assumptions an observation can be made. This being that, since the point source is located halfway through the scintillator and the fact that the detector spans the entire thickness, the entire system can essentially be viewed from the top down as a "2D" situation. Where the light propagates circularly, this 2D situation be seen in fig 16.

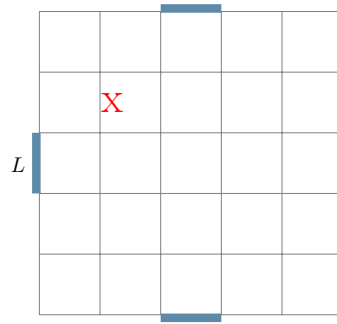


Figure 16: Top view of the scintillator with sensors on each lateral face. Muon hit is marked with a red "x", sensors are marked in blue and have a length of L .

Of course, this assumption only holds when the muon hit location is in the far range and loses accuracy at near and close ranges. However, since this boundary condition was also given for the internal reflection, this suffices.

After a muon has traversed the material, the point source of light, originating from "X" propagates circularly through the scintillator. This then reaches the sensor (see fig. 17), of course the closer end of the sensor (to the source) will receive the light a fraction sooner than the farthest end. This results in a minuscule difference in attenuation, Since this difference is so small, it can be neglected.

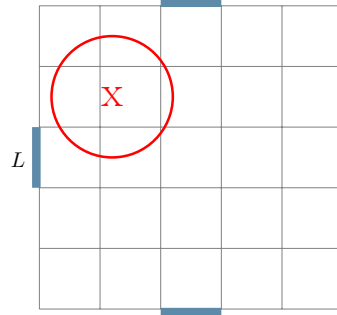


Figure 17: Top view of the scintillator with sensors on each lateral face. Light generated during scintillation ("X") propagates outward in a circle. Until it reaches a detector with size L

The fraction of photons can be found by looking at the fraction of the circle that the line covers. I.E,

$$N \propto N_0 \frac{\Theta}{2\pi} \quad (17)$$

Where Θ is the total angle covered by the sensor. To find this angle, it is helpful to look at a simplified situation, one where the muon hits in line with the direction of the sensor, this can be seen in figure 18

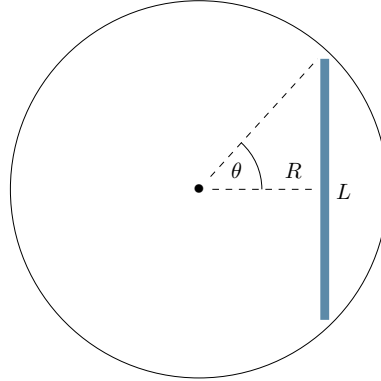


Figure 18: Top view of a simplified situation where a muon passes through a scintillator and generating a circle of photons that expand outward until they hit a detector.

Some trigonometry will show that,

$$\Theta = 2\theta = 2 \arctan \frac{L}{2R} \quad (18)$$

Here, L is the length of the sensor and R is again the distance from the muon hit location to the sensor. The factor 2 arises from horizontal symmetry,

As stated this is only true when the light is perpendicular to the sensor, However if the light comes in at an angle the effective sensor area the light "sees" is reduced, see fig. 19.

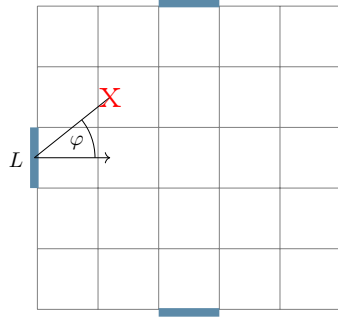


Figure 19: Top view of a scintillator, The angle between the muon's hit location and the normal vector of the sensor is denoted by φ .

Therefore, this ends up reducing the fraction of the total circle that the sensor takes up, the larger this angle, the less light hits the sensor. This angle is simply the cosine of the angle between the normal of the sensor, and the position of the muon hit. Or:

$$\cos \varphi = \frac{\vec{\mu} \cdot \vec{n}}{|\mu||n|} \quad (19)$$

where $\vec{\mu}$ is the difference in distance between the muon and the sensor given as: $[S_x - \mu_x, S_y - \mu_y, S_z - \mu_z]$ and \vec{n} being the normal vector of a sensor, where the direction the sensor is facing representing a "1" and every other value being 0. For instance, a sensor facing in the y direction would have a normal given by: $[0, 1, 0]$. Combining equations 17, 18 and 19 yields:

$$N \propto N_0 \frac{1}{\pi} \arctan \left(\frac{L}{2R} \cos \varphi \right) = N_0 \frac{1}{\pi} \arctan \left(\frac{L}{2R} \frac{\vec{\mu} \cdot \vec{n}}{|\mu||n|} \right) \quad (20)$$

Finally, this equation can be combined with eq 16 to find the total amount of photons at a distance R from the detector:

$$N = N_0 (\cos \theta_c) \left(1 + \frac{2R}{X_0} - \frac{2R}{X_0 \sin \theta_c} \right) \left(\frac{1}{\pi} \arctan \frac{L}{2R} \frac{\vec{\mu} \cdot \vec{n}}{|\mu||n|} \right) \quad (21)$$

This equation is still not complete, as other, statistical effects also play a role. This makes eq. 21 not the actual value of N , but the mean. With statistical effects determining the actual value. Hence,

$$\langle N \rangle = N_0 (\cos \theta_c) \left(1 + \frac{2R}{X_0} - \frac{2R}{X_0 \sin \theta_c} \right) \left(\frac{1}{\pi} \arctan \frac{L}{2R} \frac{\vec{\mu} \cdot \vec{n}}{|\mu||n|} \right) \quad (22)$$

What these statistical effects are, and how the full measurement setup operates, are explained in the following chapter.

3 | Setup

Now that the underlying theory has been explained, it is time to look at how one can measure the amount of light generated when a muon travels through a scintillator. For this, it is important to look at two components vital for this process, the aforementioned scintillator, as well as the silicon photomultiplier. Lets first take a closer look at the scintillator.

3.1 | Scintillator

As stated in the previous section. Scintillators convert incoming ionising radiation (muons) to (visible) light. A common type of scintillator is the aforementioned polyvinyltolulene (PVT). It is a cheap, fast and reliable scintillator that produces approximately 10 000 photons per MeV. However, there are many different scintillators, each differing in light yield, scintillation time (how fast after excitation does the light get re-emitted) and wavelength. The PVT scintillator is part of a group called plastic scintillators. These scintillators contain organic compounds such as benzene. The light gets produced when electrons in the "P" orbital (the second orbital, right after "S") get ionised and/or excited. This temporarily disrupts the so-called π bonds between two carbon atoms within a benzene ring (see fig. 20).

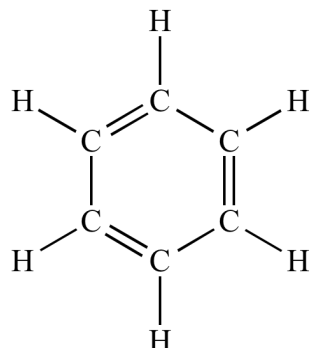


Figure 20: Benzene ring, the π bonds are the double C=C bonds. These are responsible for scintillation.

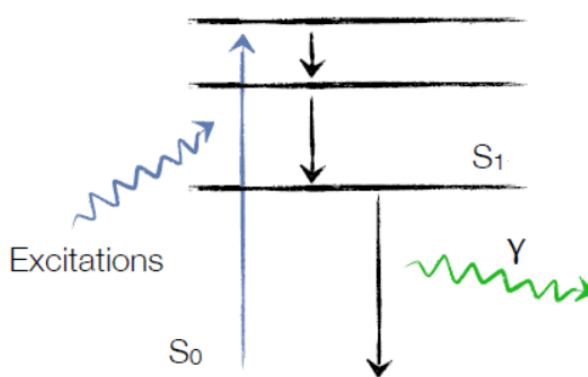


Figure 21: Schematic of scintillation, an ionising particle will excite the electrons from the ground state S_0 to a higher energy state. These will then decay to a lower energy state without emitting light, often through atomic oscillations. Afterwards they will decay again from S_1 down to the ground state emitting scintillation light [21] [22].

Once this disruption is restored, the molecule will emit light, usually in the low-visible to UV light, typically between 650-300 nm, with most being approximately 425 nm [21]. The full scintillation process is more complex but goes too far for this paper. A simplified figure describing scintillation can be seen in fig. 21.

There are different types of scintillators besides simply plastic and/or organic scintillators (I.E: inorganic, liquid and crystal) however these go beyond the scope of this paper and will therefore not be addressed.

The other important component to discuss is the Silicon photomultiplier, or SiPM. These will be discussed now.

3.2 | Silicon photomultiplier

The SiPM is a small compact array of tiny RC circuits (see fig. 22) attached to a special type of diode called a single photon avalanche diode or SPAD.

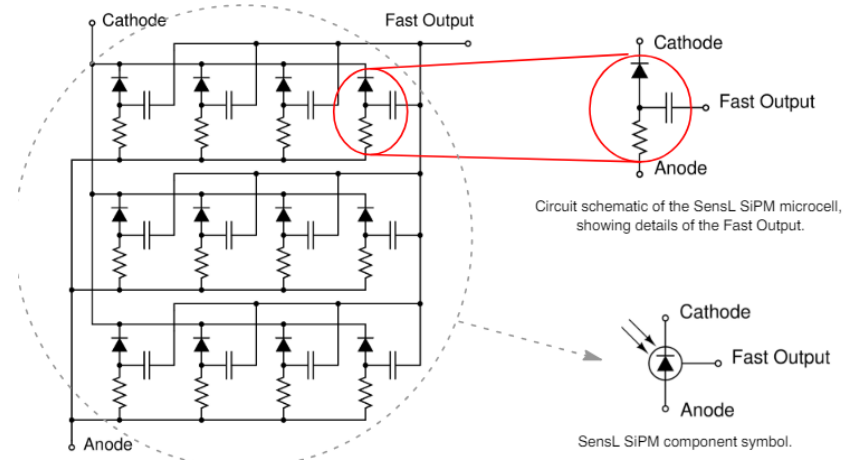


Figure 22: Simplified diagram of the components of a silicon photomultiplier. Often there are hundreds or thousands of microcells, each being only a few μm wide [23].

SPAD's are special diodes that operate just below the breakdown voltage (maximum voltage a diode can stop before conducting current), this balance between not conducting and conducting can easily be disrupted if a photon were to hit and ionise an electron. This causes an electron to get free, and a vacant hole to be left behind. This so-called electron-hole pair causes a results in a charge flow from, in other words, a peak in current before normalising again (see fig 23).

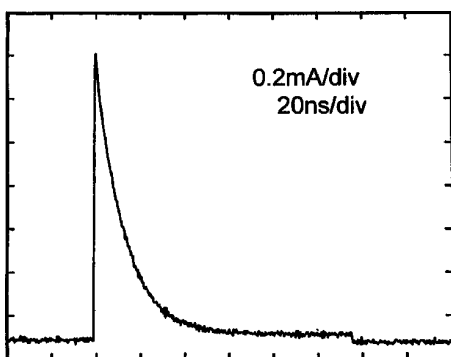


Figure 23: Pulse of a single photon avalanche diode, usually the SPAD pulse is in the range of 1-2 mA.[24]

during this " cooldown" after the initial pulse, the SPAD cannot pulse again. Therefore it is not very useful to actually count multiple photons, as these often arrive at the same time. This is why a Silicon photomultiplier is used. Many of these SPAD's added up will produce a larger pulse with each firing of an SPAD. Meaning that, in theory, a single SiPM could detect up to hundreds of thousands of photons, but also still detect singular photons. Typically a scintillation will produce a few thousand photons, where a couple hundred will reach the detector following eq. 21. However, often the actual amount of photons measured lies far lower, typically at a few dozen. This is due to effects of both photon detection (quantum) efficiency as well as Poissonian statistics. Both of these will be discussed briefly.

Quantum and photon detection efficiency

Quantum mechanics is statistical in nature. This includes the aforementioned ionisation of the breakdown electrons. This is governed by two things, the quantum efficiency and the photon detection efficiency. In short, the quantum efficiency (QE) is defined as the probability that a photon will create an electron-hole pair.

The photon detection efficiency is the probability that single photon will be detected, so after an electron hole pair is generated. There is a chance that this causes an avalanche and thus a pulse.

These two values are often combined into a general " photon detection efficiency" (PDE). Often written as either a percentage or a value between 0 and 1. This value is heavily dependent on supply voltage and usually ranges somewhere between 30 and 60 percent [23].

This, however is not the only statistical effect of photon detection. Another component is Poisson statistics, this will be discussed now:

Poisson statistics

The quantum efficiency is an inherent effect from the specific detector. However, the amount of photons that reach the detector is completely independent from this and is governed by the Poisson distribution [25]:

$$P_N = \frac{\langle N \rangle^N}{N!} e^{-\langle N \rangle} \quad (23)$$

Here, $\langle N \rangle$ is the average amount of photons reaching the detector (eq. 22) and P_N is the probability that N photons get measured.

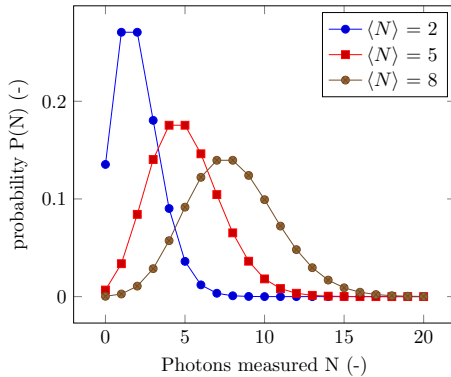


Figure 24: Poisson distribution of different values for N

As can be seen, for a large value of $\langle N \rangle$, it approaches a Gaussian distribution with a mean at $\langle N \rangle$ and a standard deviation of $\sqrt{\langle N \rangle}$.

Now that both components are discussed, it is time to look at how these can be combined to construct a detector.

3.3 | Measurement setup

Due to time constraints, only a simple detector capable of roughly approximating a position will be made. No angle determining shall be done. The goal is simply to build a rudimentary proof of concept that can be used to verify the eventual model that will be made (section 4). This way, the model can then be used to extrapolate and find any desired positional resolution using a specific area and amount of sensors.

With this in mind. The detector consists of four 3x3mm ONSEMI SiPM's attached to each lateral face (all sides except top and bottom), each of which is first amplified and then connected to the oscilloscope (OSC in fig. 25). The SiPM's run on 28 V and the amplifiers run on 5 V. The scintillator type was unfortunately unknown, however due to the fact that most plastic scintillators are approximately equal to eachother, this will not have a strong influence on results. The dimensions of the scintillator are 9x9x0.25 cm

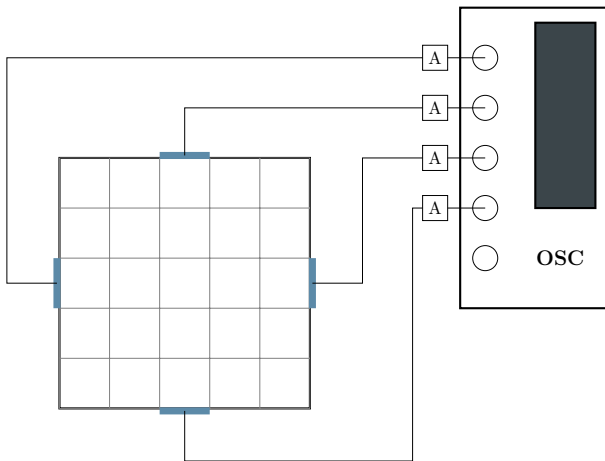


Figure 25: Schematic of the detector setup. Voltage source for the amplifiers and SiPM's are not shown. Each SiPM (marked in blue) is connected to an amplifier (A), which is connected to an oscilloscope

This detector is now able to record a voltage relating to a certain amount of photons, the scaling of which (how many Volts per photon) will be determined experimentally (see section 5). However, it will now measure photons from every single location. To precisely gather data at a single position, two smaller detectors were used. These were small scintillator blocks (0.3x0.3 active area) attached to a long light guide, where at the end sat a SiPM. these were then connected to a coincidence unit (CDU in 26), This way. If a muon passes through both detectors, the CDU will send a pulse, if only one sends a signal. It does not. These two small detectors were then placed above and below the scintillator so that a muon will always pass through the region covered by both small detectors.

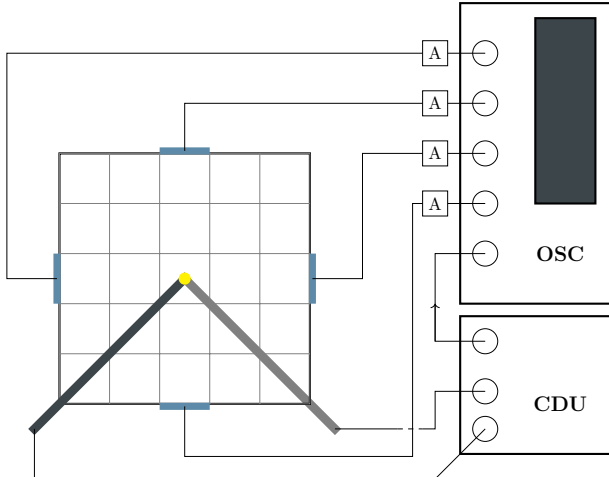


Figure 26: Schematic of the detector setup. One of the detectors is above, and one is below the Scintillator, the scintillating tip is marked in yellow, the rest of the arm is a light guide. The CDU only fires if both detectors receive a signal within a time frame of a few ms.

After the small detectors have been attached to the CDU, the output is attached to the last input from the oscilloscope. This last input is called an 'external trigger' which allows the oscilloscope to perform an action if it is triggered. In this case that would be to save the data if a muon passes through.

However, a measurement setup without anything to verify and predict its results with is not a reliable result, therefore it is important to also construct a simulated model based on the underlying theory discussed previously. This also gives an opportunity to create an algorithm able to accurately determine the impact location of the muon. This will be done in the following section.

4 | Model

This section will discuss both the different components of the model, as well as the expected result from each. This section also talks about different algorithms used to determine the position and which ended up being the most efficient. However to get to that point. equations: 1, 3 and 22 as well as the statistical effects explained in section 3.2 have to be simulated first.

4.1 | Modelling the theory

First off, it is important to choose a language and platform to create the model in. There were two options, either GEANT-4, a robust platform written in C++ specifically designed to analyse the passage of subatomic particles through matter [26]. However, this would take a serious time investment to learn and understand properly. Given the fact that creating a simulation will take time on top of having to learn a new language in a relatively short time-frame. It was decided to go for the second option, python. This also allows for gaining a more in-depth knowledge of the physics behind muon detection.

Now that the language has been chosen, it is time to model the first part of the process, the scintillator. For this, as depicted in 25, four SiPM's are placed around the lateral faces of the scintillator (see fig. 27).

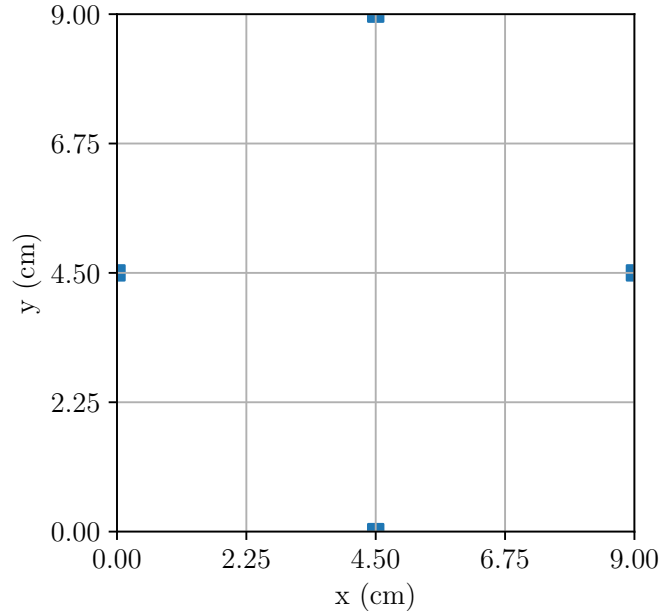


Figure 27: Top down view of the modelled scintillator with SiPM's on each lateral face.

Now that the detector is made, the core physics of a muon impact can be simulated. For this, the first step is modelling the Bethe-Bloch equation (eq. 1).

As stated before, the only energy losses accounted for are ionisation losses at low-mid GeV's. Any higher-order effects are generally exceedingly rare for cosmic muons.

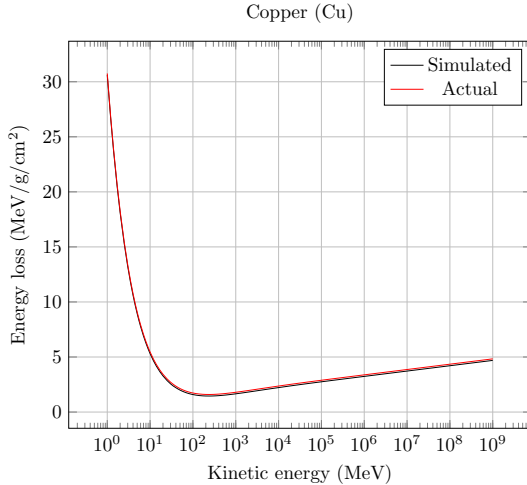


Figure 28: Simulated Bethe-Bloch versus actual Bethe-Bloch in copper on a semi-log scale.

As can be seen, both functions are in close agreement. With the minimum ionising point only differing 4 % between the simulation and actual value. This small error can come from many sources and is therefore difficult to pinpoint what is causing it.

Now that the Bethe-Bloch is deemed reliable, the next step is modelling the landau distribution (fig. 7)

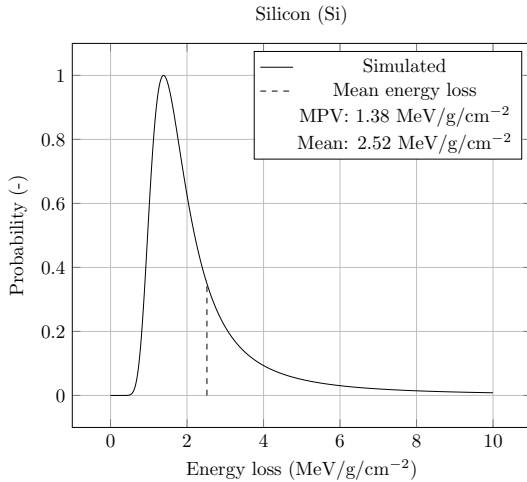


Figure 29: Simulated Landau distribution in silicon for a 10 GeV muon. The peak, or most probable value (MPV) sits at $1.38 \text{ MeV/g/cm}^{-2}$ and the average is at $2.52 \text{ MeV/g/cm}^{-2}$.

Unfortunately, no full measured dataset for the landau distribution was found. Luckily, some data about the ratio between the most probable and mean energy loss could be found. Through silicon, a 10 GeV muon has a most probable energy loss at 62 % of the average energy loss [2]. This means that this ratio between MPV and mean should be the same for the simulated result. For the simulated result it comes out to 55%. This difference is most likely due to error propagation from the Bethe Bloch.

Due to these small error percentages. It can be assumed that both the Bethe-Bloch and the landau distribution are accurate enough to create a model that will give an accurate result.

4.2 | Expected result

Now that the theory is deemed to be accurate. The model can simulate a muon scintillation anywhere on the scintillator. This produces an amount of light that propagates through the scintillator following eq. 22, in fig. 30, the average amount of photons hitting a detector, accounting for a quantum efficiency of approximately 38 %, is shown for a range of distances from 1cm all the way to 15cm.

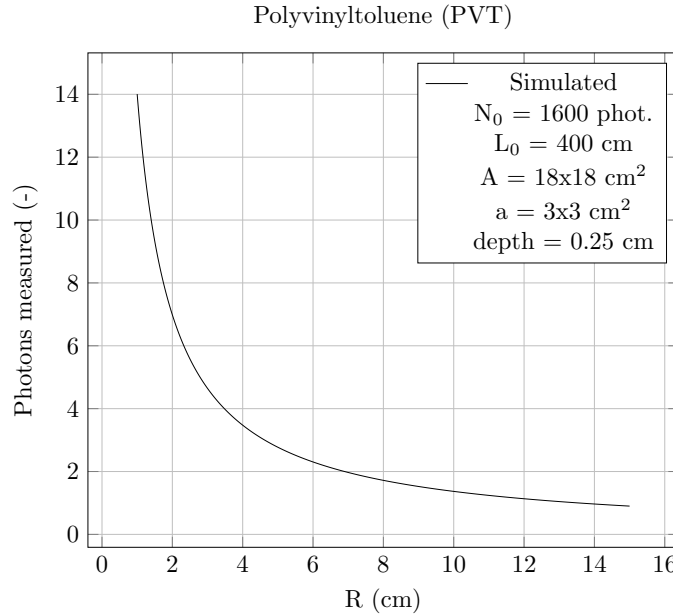


Figure 30: Average amount of photons measured as function of distance given by eq. 22.

As can be seen, the result is proportional to $1/r$, this expected result will be verified in section 5.1. What is also important to note, is that it is clear that a small thickness (such as 2.5mm as shown above) does not yield that many photons even at close distances to the detector. This shows that it is preferable to have a larger thickness.

Now that it is known how many photons will be measured over a certain distance, the position determining algorithm can be chosen. This will be discussed in the following section.

4.3 | Position determining

There are a few different methods of determining the position of a muon impact in a scintillator. An example would be using time of flight (TOF), I.E. measuring a time difference and using it to find the impact location. In this case, it was chosen to use the light yield of each SiPM, therefore allowing for less expensive and 'slower' electronics.

There are also several different ways to use the "light profile" of a sensor to determine the impact position: iterative processes, numerical ones, and possibly even a neural network [27]. Taking into account all these aspects, a fitting procedure was chosen. This will now be explained.

Suppose a muon hits the detector in fig. 27 at some position $\mu = (\mu_x, \mu_y)$,

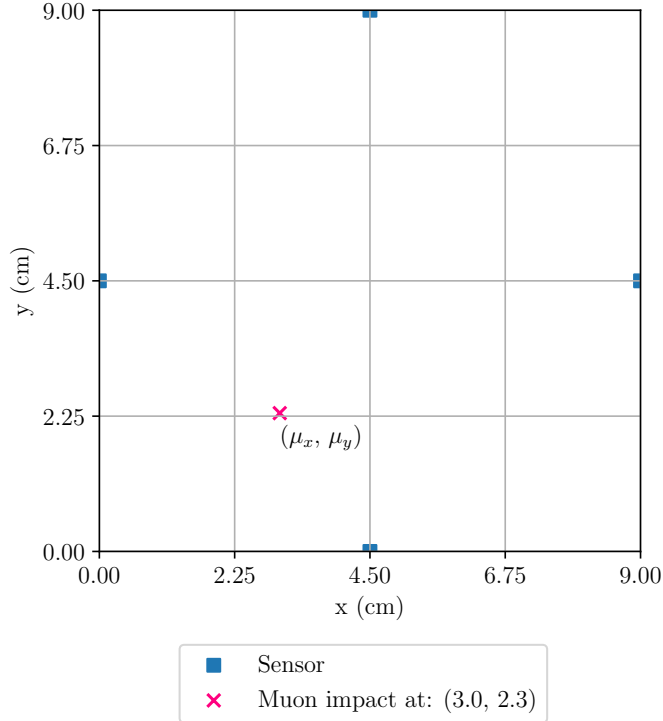


Figure 31: Top down view of a modelled scintillator with four SiPM's (marked in blue) on each lateral face. A muon impacts the detector with some arbitrary x and y positions.

From equation 22, the number of photons on every sensor can be determined. Since the amount of photons on every sensor is dependent on the same muon hit location (a different hit location would yield a different amount of photons on every sensor). It can be written as a coupled set of equations:

$$\left\{ \begin{array}{l} \langle N_1 \rangle = N_0 (\cos \theta_c) \left(1 + \frac{2R_1}{X_0} - \frac{2R_1}{X_0 \sin \theta_c} \right) \left(\frac{1}{\pi} \arctan \frac{L}{2R_1} \frac{\vec{\mu} \cdot \vec{n}_1}{|\mu| |n_1|} \right) \\ \langle N_2 \rangle = N_0 (\cos \theta_c) \left(1 + \frac{2R_2}{X_0} - \frac{2R_2}{X_0 \sin \theta_c} \right) \left(\frac{1}{\pi} \arctan \frac{L}{2R_2} \frac{\vec{\mu} \cdot \vec{n}_2}{|\mu| |n_2|} \right) \\ \langle N_3 \rangle = N_0 (\cos \theta_c) \left(1 + \frac{2R_3}{X_0} - \frac{2R_3}{X_0 \sin \theta_c} \right) \left(\frac{1}{\pi} \arctan \frac{L}{2R_3} \frac{\vec{\mu} \cdot \vec{n}_3}{|\mu| |n_3|} \right) \\ \langle N_4 \rangle = N_0 (\cos \theta_c) \left(1 + \frac{2R_4}{X_0} - \frac{2R_4}{X_0 \sin \theta_c} \right) \left(\frac{1}{\pi} \arctan \frac{L}{2R_4} \frac{\vec{\mu} \cdot \vec{n}_4}{|\mu| |n_4|} \right) \end{array} \right. \quad (24)$$

From this, it can be seen that a large quantity of variables are simply constants that can be calculated, with a few exceptions: N_0 the amount of photons created during scintillation, μ the vector notation for the muons' impact location with respect to each sensor, $[S_{x:1,2,3,4} - \mu_x, S_{y:1,2,3,4} - \mu_y]$ (see section 2.4), and R_i the distance from the sensor to the muon, which can also be written as:

$$R_i = \sqrt{(S_x^i - \mu_x)^2 + (S_y^i - \mu_y)^2} \quad (25)$$

where S_x^i represents the sensor x location for the i th sensor. Idem for S_y^i . With this, it is clear that the coupled equations in eq. 24 only have three unknowns; μ_x , μ_y and N_0 .

To find these unknowns; it is helpful to simplify the system to a one dimensional line with a single sensor at one end of the scintillator (see fig 32)



Figure 32: Top down view of a one dimensional scintillator, with SiPM's (marked in blue) on each end.

From this, it can be seen that equation 25 simplifies to $R_i = S_x^i - \mu_x$, as there is no y-coordinate on a one dimensional scintillator. Supposing that a muon hit occurs along this one dimensional scintillator, it should, logically, still follow the light propagation in eq 24, except in this case, the only two unknowns are μ_x and N_0 . Supposing that each sensor measures some amount of photons N_1 and N_2 , considering that both the left, and right sensors should fall on the same line: μ_x and N_0 can therefore be adjusted or "fitted", to give the desired result as to where N_1 and N_2 are both on (or as close to) the same curve.

Another way of visualising it is by using fig. 30. Both N_1 and N_2 should fall somewhere along the same curve. To make sure this is the case, μ_x and N_0 can be adjusted and fitted until N_1 and N_2 are as close to the curve as possible.

Of course, not only does this work for a 1D situation, but also for the 2D situation in figure 31. This time, there is just one extra fitting variable that needs to be accounted for. Doing this "tuning" and fitting by hand would take an unreasonable amount of time. Conveniently enough, a package within Python, namely Scipy, already incorporates such a curve fitting procedure, which even allows for the user to add bounds to x_0 and y_0 for even greater accuracy [28].

This curve fitting algorithm can now be used to find the muon hit location on a scintillator plate not only in one dimension, but two as well. Implementing this algorithm yields the following result:

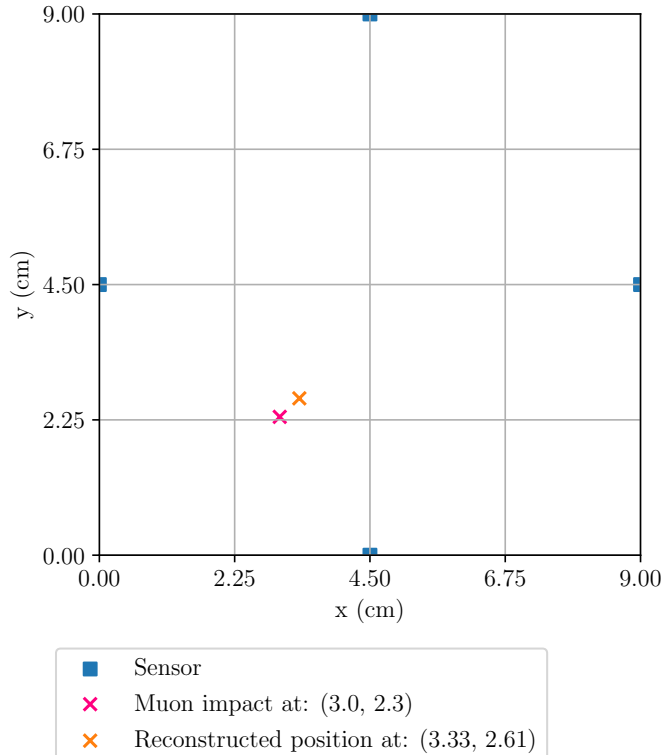


Figure 33: Top down view of a modelled scintillator with four SiPM's (marked in blue) on each lateral face. A muon impacts the detector with some arbitrary x and y position, which is then reconstructed using a curve fitting algorithm.

As can be observed, this fitting procedure is an elegant solution, that is able to easily reconstruct and "find" the hit location with relatively minimal information (only knowing the light yield for each sensor and the sensor locations). Any errors and deviations stem from the inherent randomness in both quantum efficiency, as well as Poissonian statistics, therefore causing a fluctuation such that more, or less photons can be measured at every detector and, thus, skewing the result.

If this algorithm gets repeated a certain number of times, the position resolution, which is defined as the standard deviation, can be determined. The smaller this value is, the higher the accuracy of the detector is.

Consider 10 000 repeated positional measurements of the same impact, with the only changes being statistical fluctuations; therefore muon energy, location and angle are all constant, while quantum efficiency and Poisson stochasticity are not.

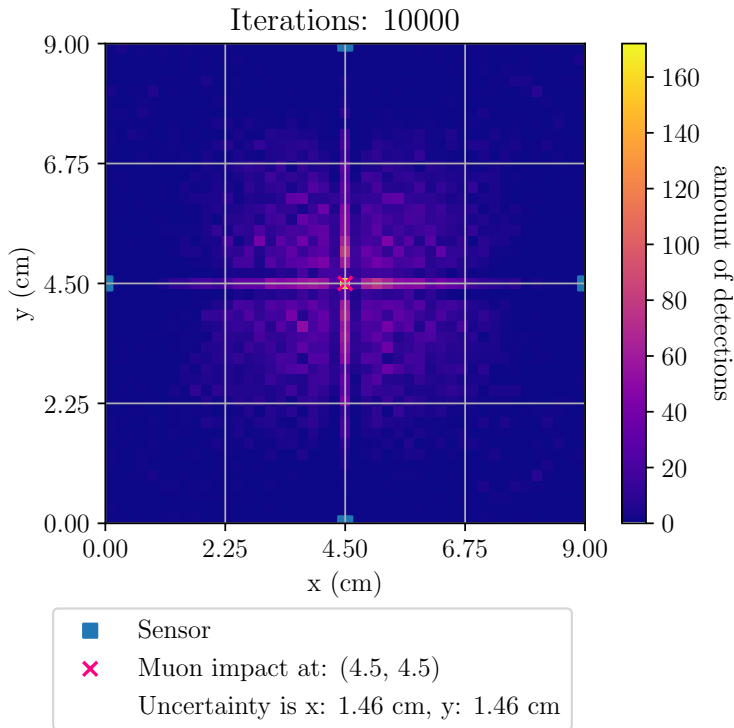


Figure 34: Heatmap of 10 000 reconstructed muon hit locations at the centre of the scintillator.

As can be seen, there is a rather large uncertainty in both x and y, with 68% of the data (1σ) falling within 1.46 cm. Although this is a result far from the desired 4 mm (4 mrad) resolution, it is still a result that can be verified with measurements.

Of course, both scintillator thickness and surface area will greatly impact this positional uncertainty. Besides verification of the model, the effect of thickness and surface area will also be discussed in the following chapter.

5 | Results

This chapter discusses the results found with both the verification of the model, this chapter will also show what is needed for the desired accuracy as well as the creation of a crude, but functional, muon detector.

5.1 | Verifying the model

Initially, the mean number of photons as function of distance to a SiPM was tested and compared with the results found in fig. 30. Several distances ranging from 1cm all the way to 15cm were measured. This can be seen in fig 35

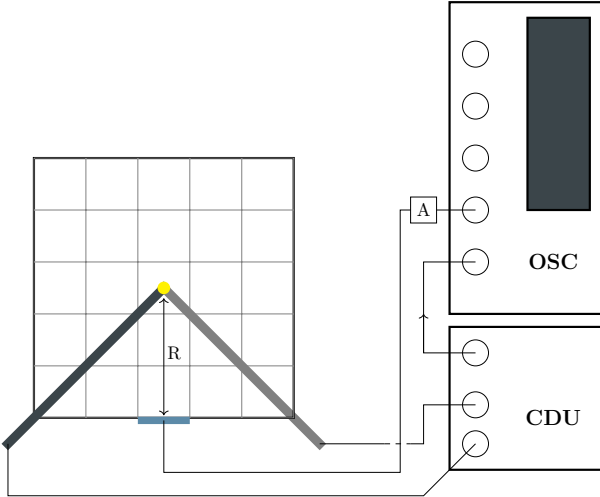


Figure 35: Top down diagram of the setup to verify the mean number of photons as function of distance. The long scintillator tips (marked in yellow) attached to the CDU allow for precise measurement at specific distances.

The SiPM, is at some distance R away from the Scintillating tips. This ensures that the distance to the SiPM is constant, and therefore allows precise measurement of the average amount of photons at this distance R . Each time a SiPM pulses, it has a characteristic peak (see fig. 36). This amplitude is directly related to how many photons it has measured.

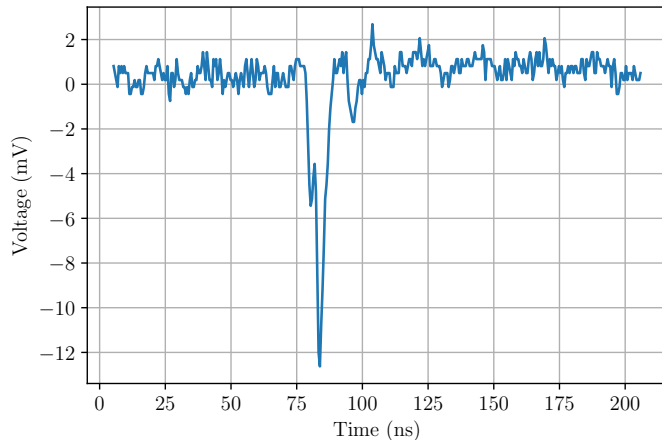


Figure 36: A SiPM pulse after detecting photons from $R = 7.5\text{cm}$ away. The amplitude of the peak corresponds to a certain number of photons that were detected.

To find the mean amount of photons hitting the detector, the amplitude of the peak can be recorded at every pulse. The primary cause of fluctuations in the measured voltage (photons) comes from the stochasticity in energy loss (see section 2.3.1), which is the landau distribution. Therefore, if a histogram is made of all the measured amplitudes, a landau distribution should appear:

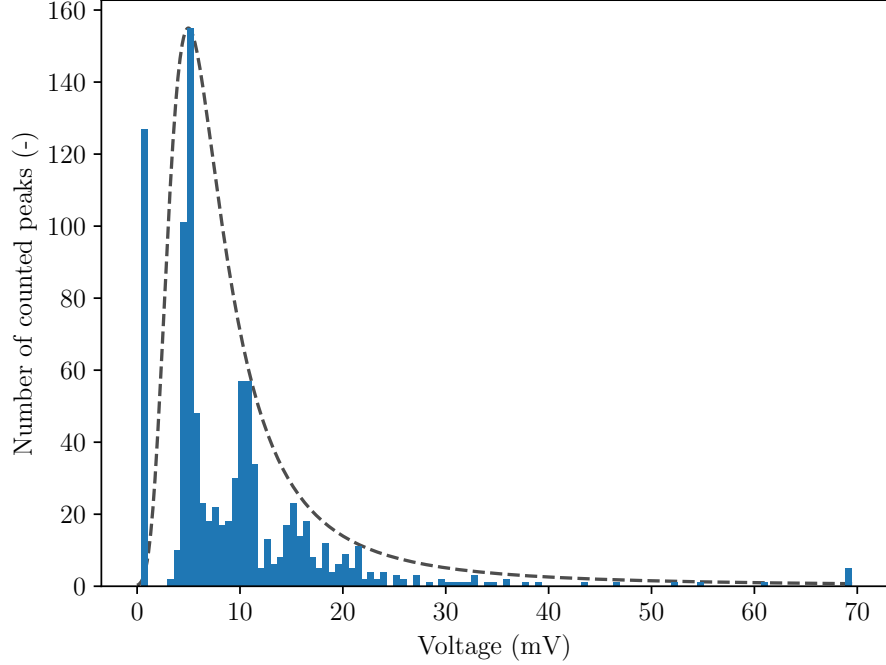


Figure 37: A histogram displaying 929 measured peaks of different voltages. Measured from a distance of 10cm. A landau distribution was fitted to guide the eye.

As expected from the theory, it seems to follow a landau distribution. There appears to be a discretisation effect, where, aside from Gaussian noise. Only a specific voltage will get measured for a specific amount of photons measured, I.E; N photons measured will yield a peak of aN where a is a factor that states how many mV each photon is. This voltage per photons ratio can be found from the histogram in fig 37, ignoring the initial peak (noise counts), each subsequent peak is at approximately 5 mV, 10 mV and 15 mV. To now find the voltage per photons ratio, it has to be assumed that each of these peaks is 1,2 and 3 photons respectively.

Recording these peaks in the histogram and taking the average of their distances yields a voltage per photons ratio of approximately 5.02 mV. Meaning that every 5.02 mV is a single photon. Thus, fig. 37 can be converted into a histogram showing how many photons were measured how many times. This can be seen in fig. 38.

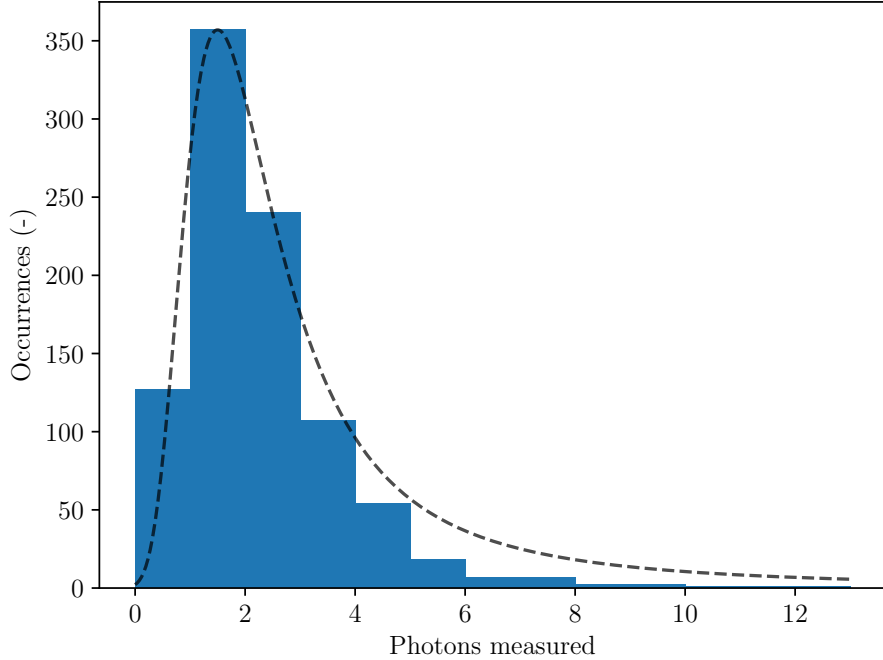


Figure 38: A histogram displaying 929 measured peaks of different photons. Measured from a distance of 10cm.

This, as expected, also follows a landau distribution, with the most probable amount of photons measured being 1, with an average of 1.82 photons.

This result can be done for a variety of different distances, all distances measured can be seen in table 1. All values used are the average.

Table 1: Table showing all measured distances and the simulated photon yield at each distance, the uncertainties in measured photons arose from the coincidence unit (fig. 26) having a surface area of approximately $0.5 \times 0.5 \text{ cm}^2$, the reason for the larger uncertainty at 5 and 10 cm is due to using a larger coincidence setup with a $1 \times 1 \text{ cm}^2$ area.

$R \text{ (cm)}$	$\langle N_{meas} \rangle$	$\langle N_{sim} \rangle$
1.0 ± 0.25	13.55	± 0.54
2.5 ± 0.25	4.921	± 0.30
5.0 ± 0.50	3.124	± 0.73
7.5 ± 0.25	2.490	± 0.16
10 ± 0.50	1.823	± 0.77
15 ± 0.25	0.992	± 0.13

In fig. 39 these results are plotted and fitted accordingly:

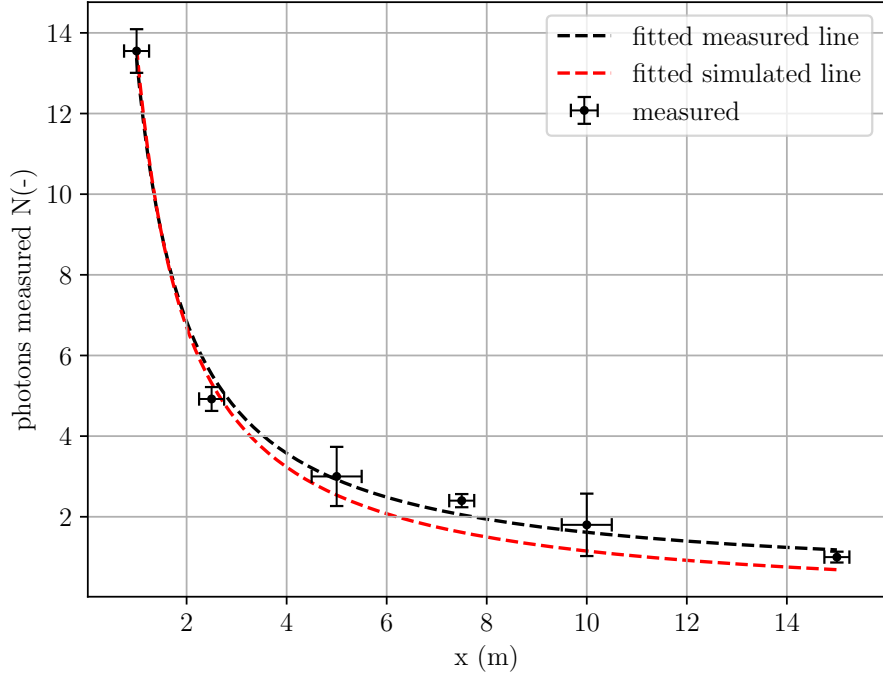


Figure 39: Most probable amount of photons measured as function of distance.

As can be seen, there is a close agreement with the simulated data found in section 4.2, with only a minor deviation at larger distances, this is best explained by the linear approximation for the light attenuation that was done in section 2.4, despite this, most data falls within its respective uncertainty. This is a strong indicator that the model can be trusted to generate data for testing the position determining algorithm, this will be discussed in the following section.

5.1.1 | The position determining algorithm

The algorithm can be verified by using the setup in fig. 26 by measuring the peaks of every SiPM attached to the scintillator. Then, by following the same process shown above. The total amount of photons for each SiPM can be found. This can then be done every time a muon triggers the coincidence unit. In fig. 40 both the measurement as well as the simulation heatmaps of the reconstructed positions are shown.

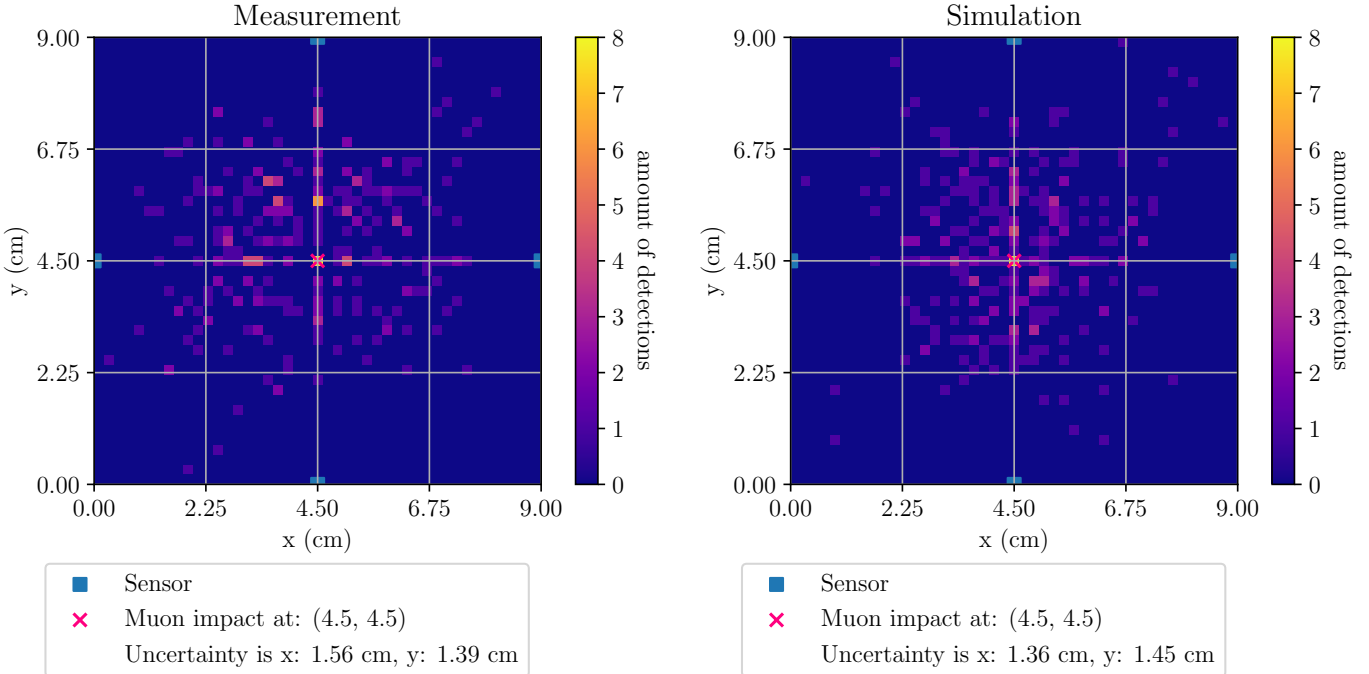


Figure 40: 281 Muon hit positions reconstructed in both Measurements and in simulation. Every muon hit goes through the same coordinate (4.5,4.5), the fluctuations occur due to landau and poissonian statistics discussed previously.

It is clear that both the Simulation and measurement data seem to agree fairly well, just as with fig. 39. There is a slight difference in both the x and y uncertainty however, this can be explained due to the rather low (281) measurements. If the measurements were done over a longer period it can be assumed that they would gradually end up at the same uncertainty in x and y.

There are many different methods and statistical tests that can be done to determine the accuracy of the model, however, since position determining appears to be somewhat Gaussian (see fig. 41). Only the standard deviation will be compared. Any other statistical test such as chi squared or a Z-test, go beyond the scope of this paper and will therefore not be addressed.

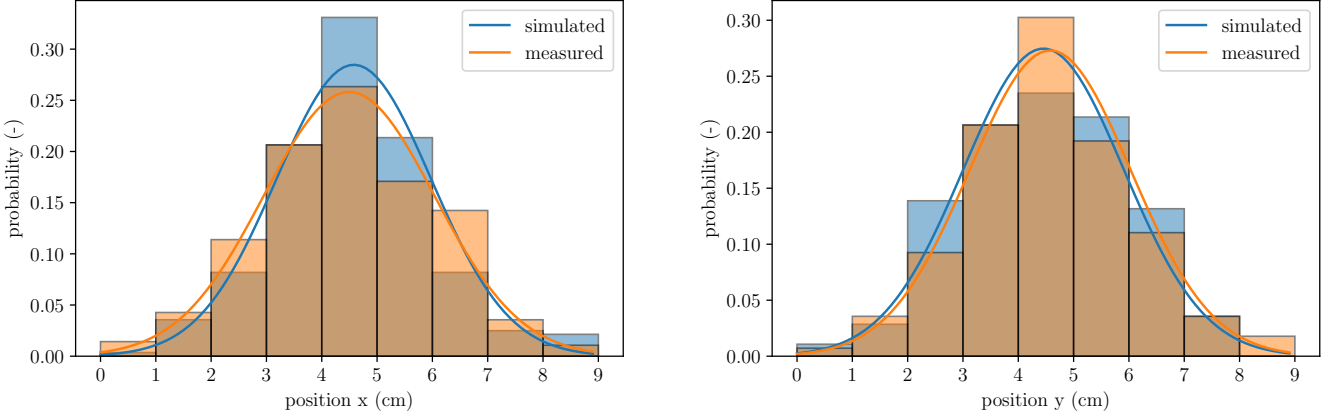


Figure 41: Normalised Gaussian of both the x and y axis, clearly showing that both have a Gaussian distribution.

As can be seen, the distributions in x and y are roughly equal. This can also be seen by comparing the total uncertainty;

$$\sigma = \sqrt{\sigma_x^2 + \sigma_y^2} \quad (26)$$

This total uncertainty comes out to be:

$$\sigma_{sim} = 1.99 \text{ cm}, \sigma_{meas} = 2.09 \text{ cm}$$

Which comes out to an error of approximately 5.03 %. With this close agreement, it can safely be said that the model works do a desired degree, and that it can be used to gain information on how σ changes with detector geometry (sensor amount, scintillator surface area and scintillator thickness). This will be done in the following section.

5.2 | Dependency of spatial resolution on detector geometry

Now that the model has been verified and has deemed to be accurate to a first degree. It can be used to find out what is necessary to obtain the result desired for practical use. This has been chosen to be on the order of a millimetre, similar to the detector used in the fukushima incident [1], which comes out to approximately 4 mm.

There are four major components to this: the scintillator type, some producing more photons than others; the scintillator depth, a thicker scintillator also produces more light; The surface area or the distance between the muon hit location and the sensor (heron referred to as side length, defined as the square root of the surface area) further away yields less photons; and finally, the number of (equally spaced) SiPM's.

For the scintillator, it was chosen to focus on plastic scintillators as these were the only type tested and verified by the model. The thickness and side length were each tested on a range from (near) zero to 1 cm and respectively. Finally four different sensor arrangements were used, namely; four, eight, sixteen and thirty-two, the way these sensors were arranged is shown in figure 42.

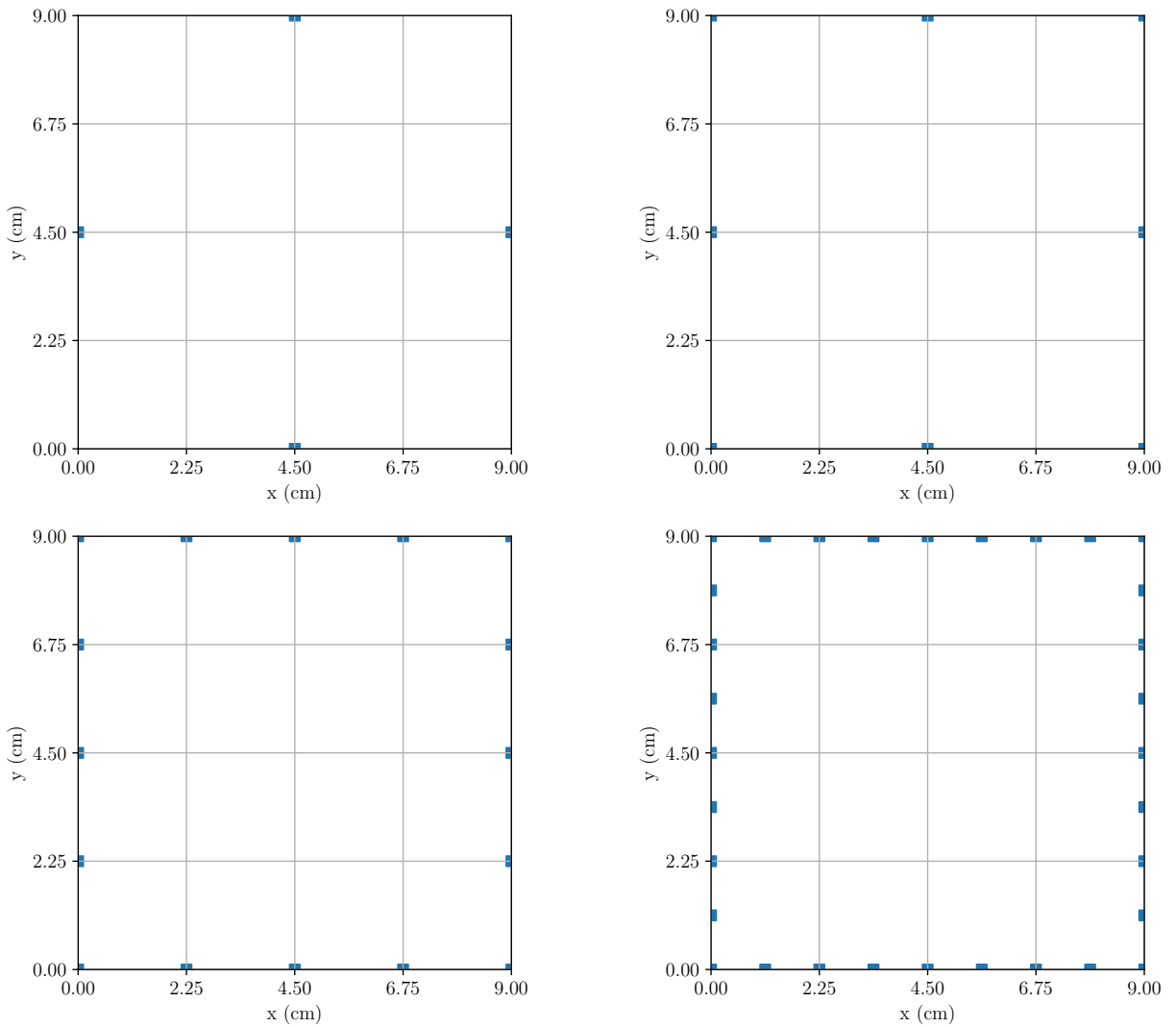


Figure 42: Top down diagram of all the sensor locations for each sensor amount (sensor marked in blue).

Now that these ranged and limits have been set, the same procedure as in figs 40 and 34 can be done for a range of depths, surface areas and sensors as given above. To reduce the time complexity only about fifty data points for both depth and surface area are simulated with each datapoint measuring the position 100 times, this is a total of 500 000 data points.

To ensure the resulting graph is smooth and not "blocky" (as will be the case with a 50x50 grid) two things can be done; one being to interpolate the 50x50 grid to be 100x100 datapoints. Another would be to perform a blur over top the dataset. This averages out the values so there is a smoother transition from one datapoint to another, effectively increasing the amount of iterations per datapoint.

Each datapoint is the positional uncertainty, belonging to a specific depth, side length and sensor amount, and is the total of both x and y uncertainties as given by eq. 26.

The scenario that is being considered is a muon hit in the centre of the scintillator, as was done during verification.

Putting this all together yields the following four graphs, each for a different sensor amount.

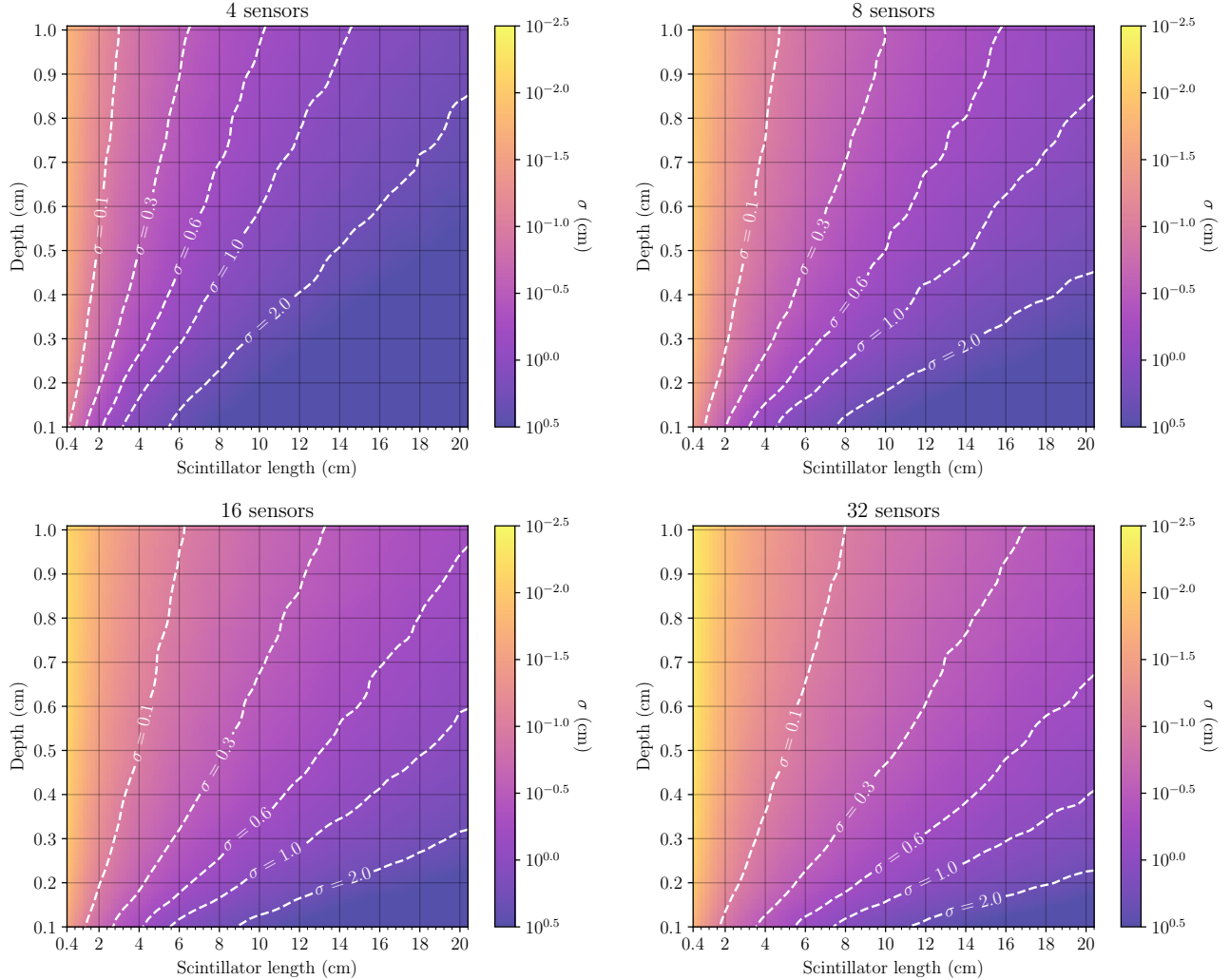


Figure 43: Graphs showing how the total position resolution σ depends on both area and depth for different sensor amounts. Colourmap was set into log scale to fit a large dynamic range.

Firstly the black dashed lines indicate different levels of uncertainty, any value for side length and depth yields the same uncertainty along this line. For instance; a 2x2x0.3 cm scintillator would have the same positional uncertainty as a 4x4x0.6 cm scintillator. However, even though they are the same. It is probably better to go with the latter option considering the doubling in aperture size, allowing for a larger viewing angle. Interestingly, a 6x6x0.6 cm scintillator with four sensors has a positional uncertainty a little below 3 mm, whereas with thirty-two sensors, it is right on the line of one millimetre precision. From these graphs, it can also be seen that it is rather difficult to obtain a sub millimetre resolution. Anything to the left of the $\sigma = 0.1$ line would be sub millimetre, and it only starts to get feasible results with higher sensor numbers. What is easier to obtain however, is 3-6 mm uncertainty, it can be seen that a scintillator of 9x9x0.75 with four sensors is a little less than 0.3 mm , only improving more when the number of sensors is increased.

These graphs allow one to quickly find what scintillator specifications they need for a specified surface area/uncertainty/depth and are, therefore, quite useful in the field of muon detection/tomography.

Now that it is possible to find what is needed to create a detector with the required specifications, it can be built using components that were available at Nikhef. This will be discussed in the next section.

5.3 | Creation of a muon detector

So far, every measurement is done semi-automated, with the oscilloscope getting automatically triggered with each muon passing. However, all the data is still read out manually. This takes a lot of time which is undesired for a proper detector. Another downside of the current setup is that only a specific location, the intersection of the two scintillating tips (see fig. 26), can trigger the oscilloscope. For these reasons, the decision was made so as to not use the oscilloscope and transition onto something more portable instead. The most important aspect of this new data acquisition system is that it must be able to be plugged into a computer (via USB). This way, the data gets directly sent to the computer and is automatically read out such that it gives a real-time feed of muons hitting the detector.

Fortunately, something similar to what is needed is already available at Nikhef, this being a set of Cosmic watches [29]. These cosmic watches are small Arduino-based systems that use simple electronics and simple software to be able to measure detect a muon. An image of a cosmic watch can be seen in figure 44:

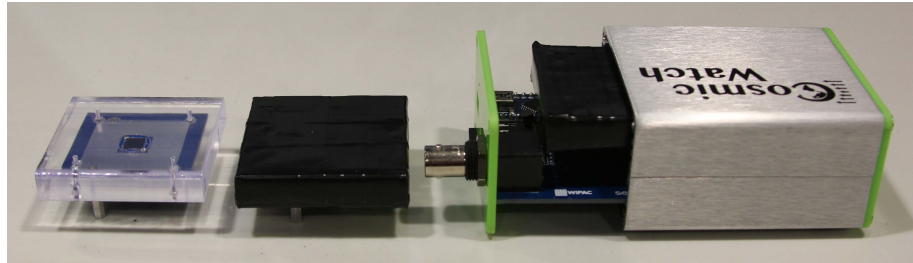


Figure 44: Side view of the cosmic watch setup. Left; SiPM attached to a scintillator on top and a PCB (silvery blue section) on the bottom. Middle; Scintillator is wrapped so that no light can enter. Right; Full cosmic watch setup. Featuring a BNC connector to allow for the output to be connected to an oscilloscope and a USB connection to connect it to a PC [29].

Typically, these cosmic watches are used by university students to measure the muon flux at sea level or other simple experiments. The plastic scintillator included yields on average 10 000 photons each time a muon traverses the scintillator. This is more than enough to allow the SiPM to detect the muon and the effect of the rather "slow" electronics will not play a large role (since with muon flux measurements simply detecting a muon is enough). However, since in the case of the position determining, a loss of even a single photon can have large impacts on the positional uncertainty. Therefore it is important to first, characterise the cosmic watch setup, for this, a similar setup as figure 26 was used. Except in this case, the amplifying unit is removed and instead a cosmic watch is attached to every sensor.

This, however, can't be done directly, as the SiPM PCB (see fig 44) needs to be connected to the cosmic watch, and each of the SiPM's themselves need to be attached to the scintillator. For this, some wires were soldered from the SiPM to the SiPM PCB and the SiPM was attached to the larger scintillating plate.

This scintillating plate was a 9x9x0.75cm plastic scintillator. This increase in thickness compared to the previous 0.25 cm thick scintillator, also increases the amount of light measured and will thus reduce accuracy. From fig 43 it can be found that for four sensors, this detector unit will yield an ideal positional uncertainty of approximately 2.5 mm, just above the desired positional uncertainty.

For the verification of the setup, the BNC output of each cosmic watch was attached to the oscilloscope, just as before. The full setup can be seen in fig 45

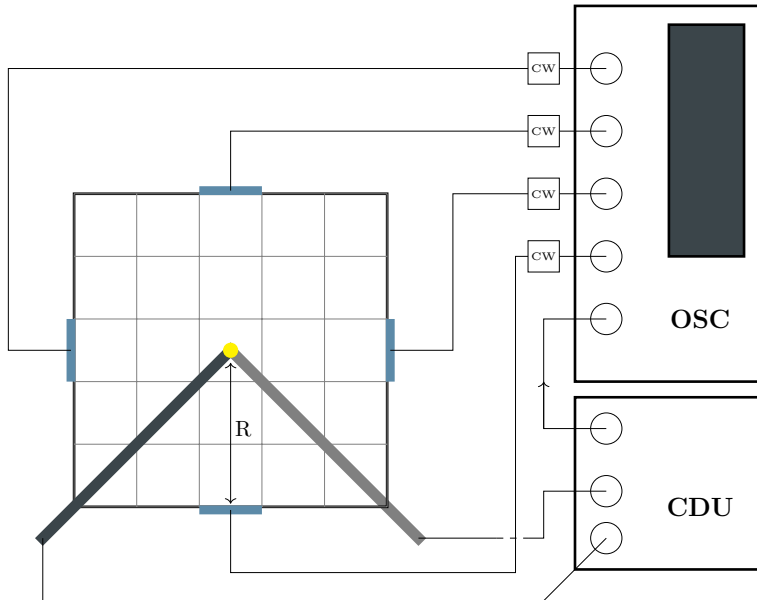


Figure 45: Top down view of the detector setup, this time the amplifiers are replaced with cosmic watches (labelled CW). The coincidence unit shall be used to verify the cosmic watches. It is important to note that the sensors are now 6x6 mm² compared to the 3x3 mm² in the previous sections.

Again, like last time, each time a muon travels through the scintillating tips, the CDU triggers the oscilloscope and records the voltages for each SiPM. Only this time, the signal first gets processed by the cosmic watch. The full explanation of the signal processing goes beyond the scope of this paper but to simplify; it receives a nanosecond pulse similar to fig 23, which it then gets "slowed down" to a microsecond pulse. Just fast enough for the Arduino to catch the signal, such a pulse can be seen in fig 46

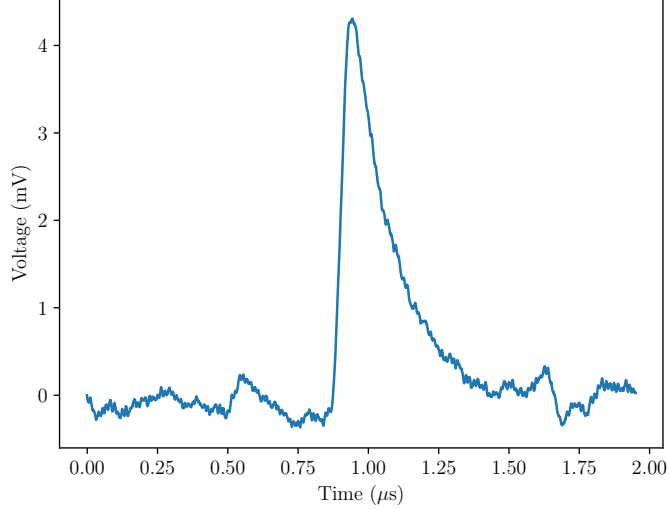


Figure 46: The SiPM pulse attached to a cosmic watch. Note how the peak is now vertical and the pulse duration is longer than in fig 36.

Each cosmic watch can differ, after all, no two sets of electronics are the same. Therefore all four cosmic watches need to be calibrated to ensure that they operate as desired. This calibration means simply multiplying each of the cosmic watches by a certain factor, so that their voltage to photon ratio (see section 5.1) are all the same. This can be done by recording muon hits on a single location where each of the sensors gives a known result. In this case, if the centre of the scintillator is chosen, the average amount of photons measured at each sensor $\langle N_{1,2,3,4} \rangle$ should be identical. Thus, by dividing one of the chosen average sensor voltages by the other three this results in a calibration factor to essentially "normalise" all measurements.

It seemed that all calibration factors were relatively close to each other, ranging between 1.07 to 1.41. After this calibration had been done, the cosmic watches could be used to verify the expected uncertainty stated prior. This can be seen in fig 47

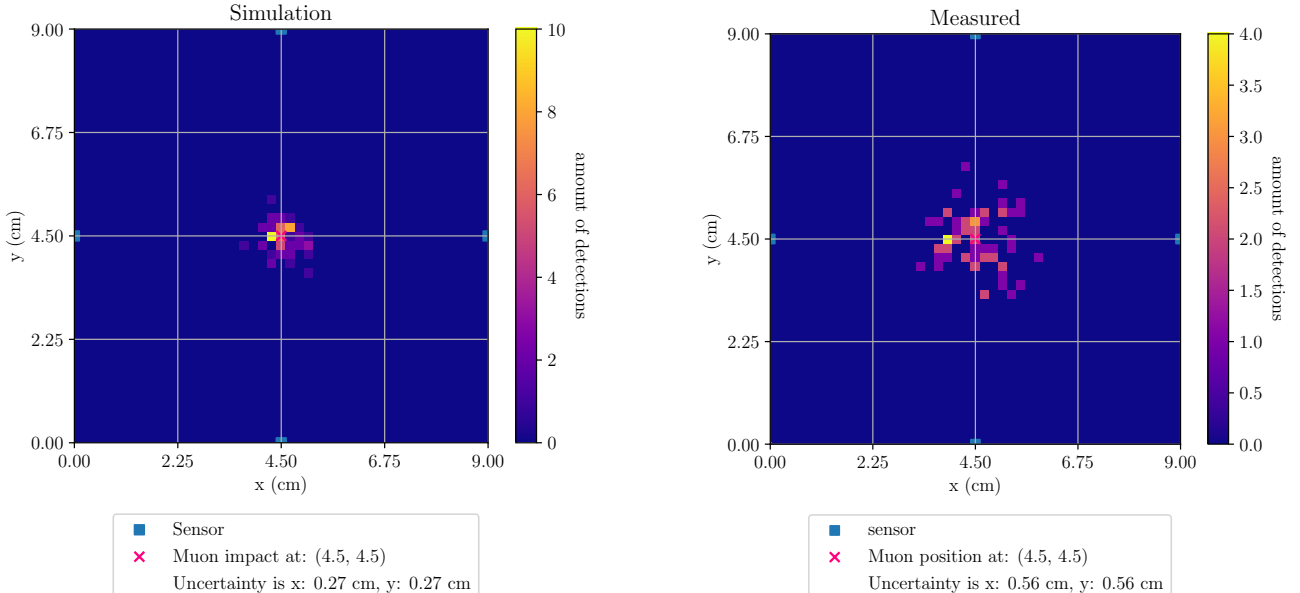


Figure 47: Heatmap of both the simulated and measured reconstructed positions, the total amount of measurements is 108.

As can be seen, there is quite a significant difference between the simulated and measured uncertainty. The measured uncertainty is approximately a factor two larger than the simulation. This can be explained due to the signal processing as well as the fact that the cosmic watches simply were not designed for this. As stated before the cosmic watches regularly measure over 10 000 photons. It is therefore not a problem if there is a slight decrease in photons measured due to signal manipulation. However, for the position determining, it is vital that as little photons as possible get lost. To show that the system does not just work at the centre of the scintillator but also at any other coordinate, the experiment shown above was redone at a different coordinate,

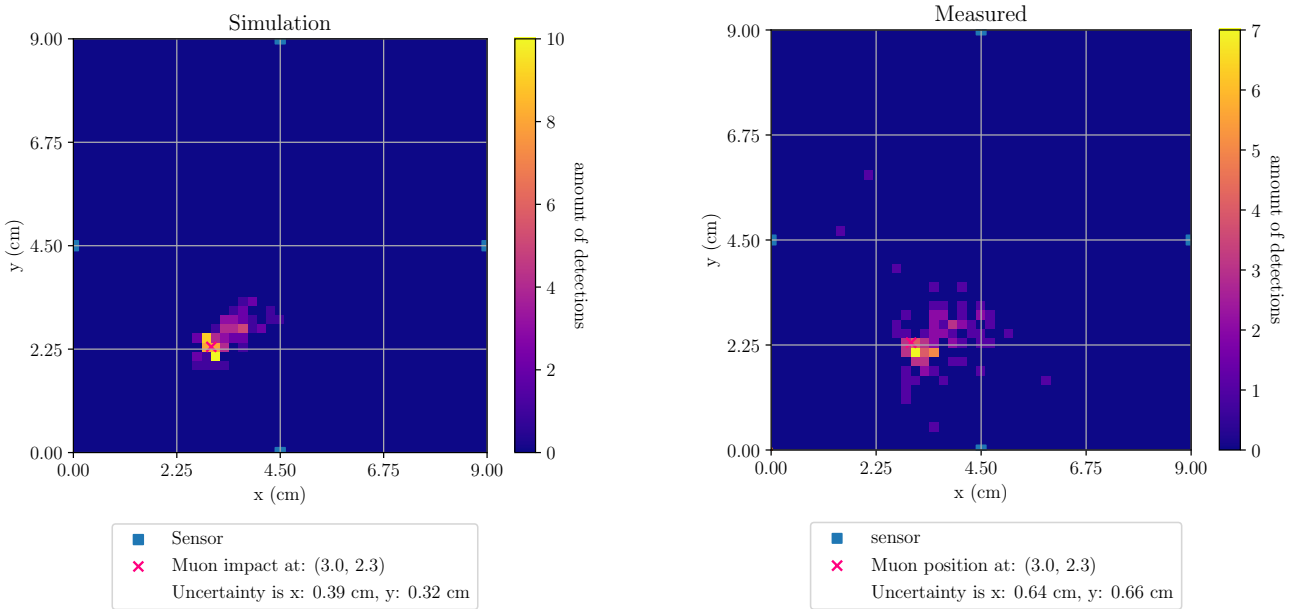


Figure 48: Heatmap of both the simulated and measured reconstructed positions, the total amount of measurements is 95.

Here too, the difference between the simulated and measured uncertainty is approximately a factor 2. With these results, it is clear that a custom-made system would be preferable. However, due to the short time frame of this research,. It was unfortunately not possible to design a custom data acquisition system; hence, these cosmic watches, despite their higher uncertainty, were still being used.

Now that it is shown that the cosmic watches can be used as simple data acquisition systems, it is possible to create a positional detector that displays the reconstructed muon hit in real time. This was done by connecting each of the cosmic watches via USB to a laptop, which then reads out the amplitude of the peaks (see fig. 46). This amplitude can then, in real time, be used to locate the muon hit location with the uncertainty seen in figures 47 and 48. A full diagram of the setup can be seen in fig. 49.

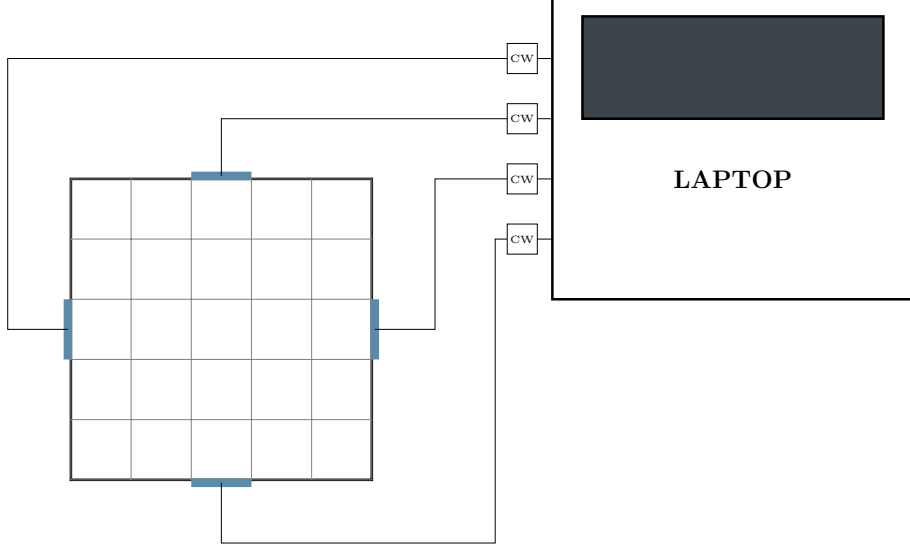


Figure 49: Top down diagram of the setup, each SiPM is connected to a cosmic watch (CW), which is attached to the laptop via USB. The laptop receives a live data stream of the cosmic watches, which send out a signal if the voltage measured by the cosmic watch is greater than the noise threshold.

Unfortunately, the cosmic watches are quite noisy, especially when used in a way they were not designed for. Due to this, to ensure only muon hits are detected, a threshold level had to be chosen. This was done by verifying with the oscilloscope whether the reconstructed position came from a muon or if it was in fact a faulty noise hit. This process was then repeated until no more noise hits were detected by the oscilloscope.

From this point onward it was decided to record each muon hit to test the full detector, and to see what the muon background radiation was like. In theory, a heatmap of reconstructed muon positions should be nearly uniform. Although the measurement was done inside a building, this should not affect a simple positional measurement. The total measurement time was approximately 40 hours and yielded 10 232 muon detections, the heatmap of reconstructed positions can be seen in figure 50.

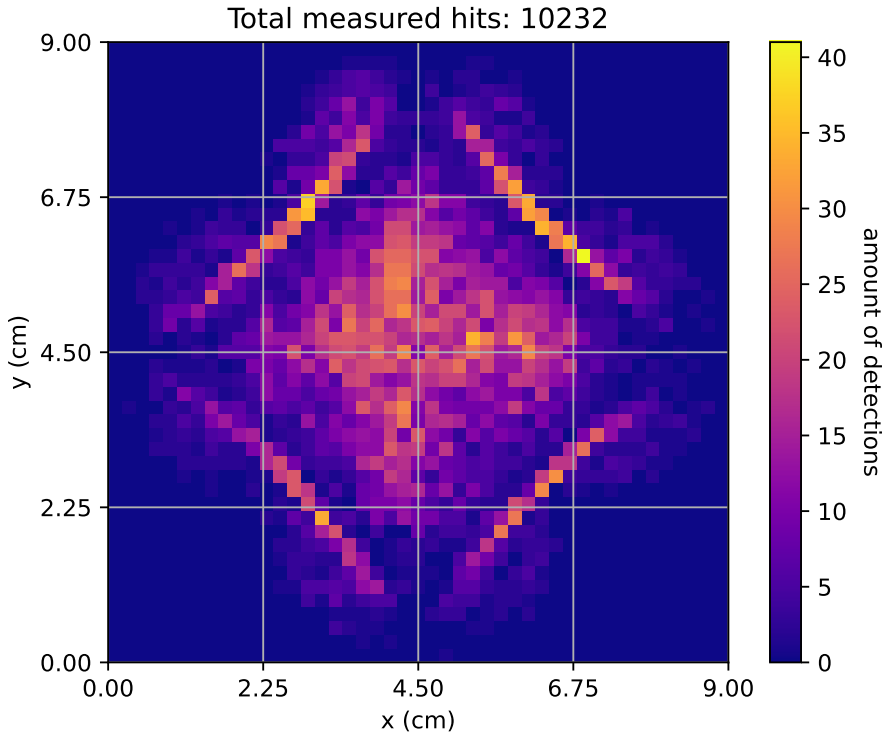


Figure 50: Heatmap of 10 232 reconstructed muon hits over the entire scintillator. Interestingly, a pattern appears to have emerged.

Curiously, a pattern appears to have emerged. Something that, as stated before, should not have happened. At first glance, this "blindness" appears to have been caused by the cosmic watches not operating properly, either due to the noise threshold being too high or otherwise. However, on closer inspection a more interesting answer arose.

The angle the muon makes with the two nearest SiPM's is so large that the measured light is drastically reduced, resulting in significantly altered reconstructed positions. These alterations can be seen when fig 48 is repeated for a more extreme location, very close in the corner such as in fig 51:

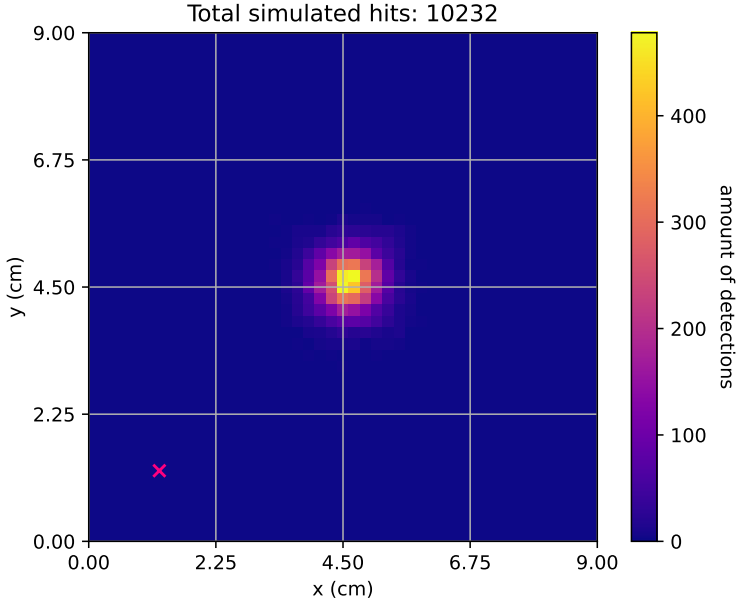


Figure 51: heatmap of 10232 reconstructed muon hits, at $\mu_{x,y} = 1.25, 1.25$. Interestingly, they do not seem to be accurate.

As can be seen, the reconstructed positions are vastly different from the actual position. The angle to the nearest two SiPM's is now so steep that the effective area the light "sees" (see section 2.4) is so small that the total light landing on the detector is reduced, which causes errors like in figure 51. To prove that this is indeed caused by this effect. Figure 50 can also be simulated and compared. If the same pattern appears in the simulation, then it means it is caused by the steep sensor angle.

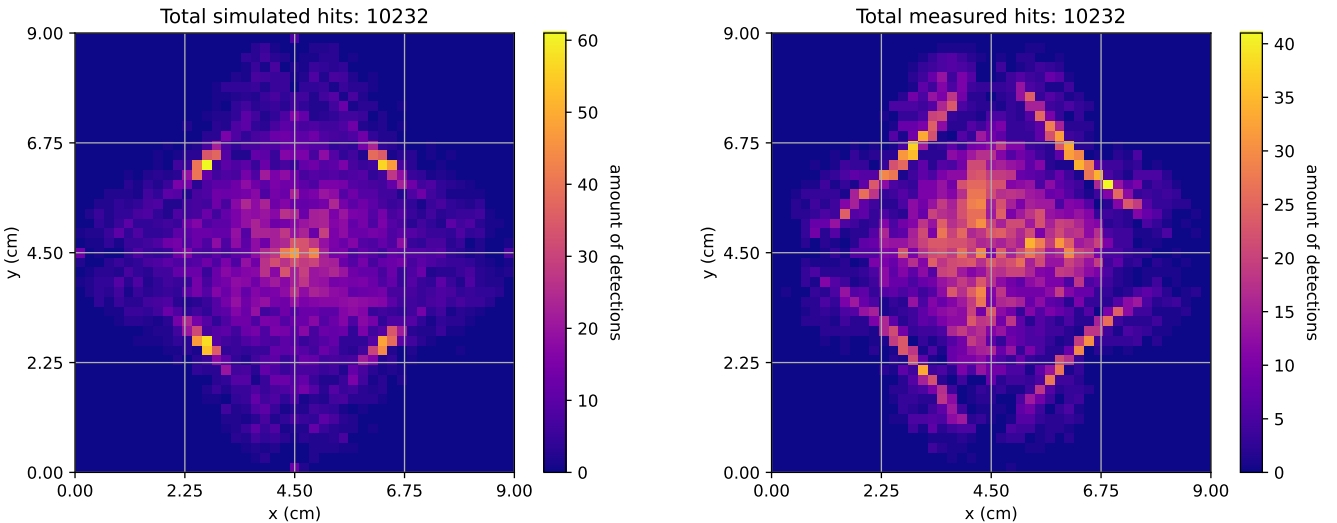


Figure 52: Heatmap of both the simulated and measured reconstructed positions over the entire detector. The pattern seems nearly identical for both.

Clearly, the pattern is also visible in the model. Therefore it is safe to assume that this steep angle effect is what is causing the pattern to appear.

Now that it is shown that the model and simulation agree with each other, it can be discussed how to solve the "blindness" in the corners.

To solve this issue, it is recommended to, instead of placing the sensors at the faces of each scintillator, placing the SiPM's at the corners at a 45-degree angle. This way, the maximum angle that the light can hit is at a 45 degree angle, instead of a ninety degree angle, since the viewing angle gets reduced from 180 degrees on the current setup to 90 degrees when the sensors are at the corners with a 45 degree inward rotation.

This can also be shown in the model if the location and rotation of the sensors is adjusted accordingly;

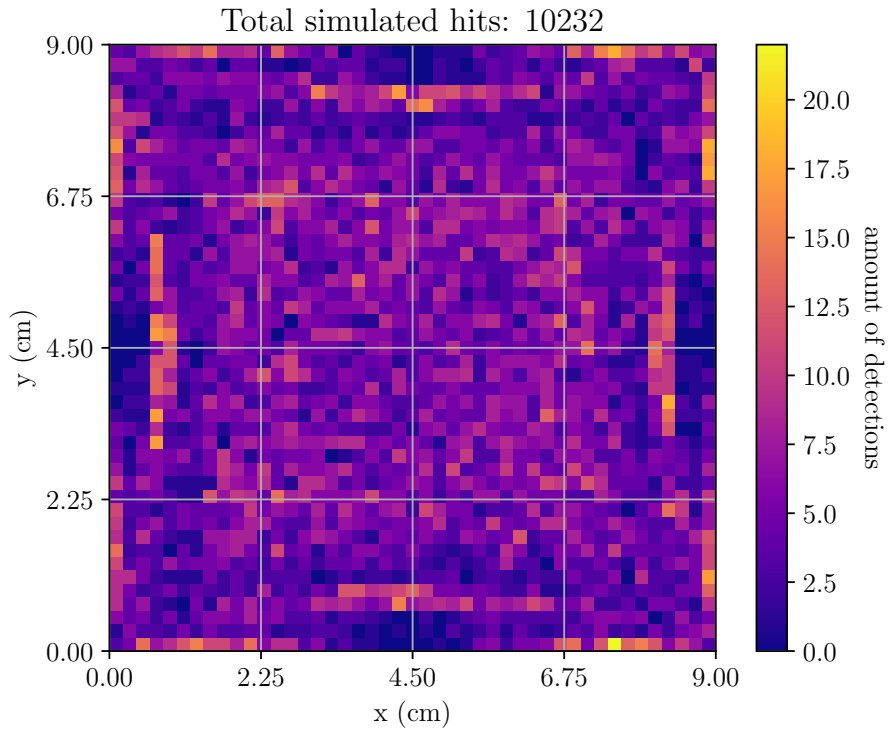


Figure 53: heatmap of 10232 reconstructed muon hits over the entire scintillator, now with the sensors at each corner. There are hardly any blind spots.

As is shown, with the sensors in the corner, it is a much more uniform distribution. There are still some small blind spots around the edges, however these are much smaller than the previous sensor locations.

Due to time and scope constraints, it was not possible to redesign the used scintillator with sensors at the corners. This, as well as further improvements and shortcomings to this paper shall be discussed in the following section.

6 | Discussion & Recommendations

In the previous section, the model was tested and verified and afterwards a fully working muon detector was made. However, some problems arose during the creation of both the model and the verification.

One of the primary inaccuracies when creating the model was the assumption that the scintillator is thin, and that therefore all the light is approximately generated at the centre. Whilst this suffices for thin scintillators and muons that do not traverse the scintillator at an angle, it does not hold when a scintillator is considered thick. Neither does it hold for when the muon travels at a steep angle. The effect of both of these have not been accounted for in the model. It is therefore recommended to analyse these sections of the model first as these are most likely the largest cause of error.

Another approximation made is that the sensor is the exact same size as the thickness of the scintillator. This makes it so that if the scintillator thickness doubles, the SiPM's surface area quadruples. This suffices for a first-order model such as the one created here, but it does not always reflect reality. This should also be a subject of further research.

Another problem encountered were the cosmic watches. These were of course never designed for such complex tasks, only being used for simple yes/no muon detection and (rough) energy estimation. These also added significant uncertainty to the setup, nearly doubling the uncertainty. During future research it is advised to spend significant time in researching a better data acquisition system. A possible solution could be a peak detection circuit attached to a Raspberry pi. Since this allows for a fully remote operation and would not need a PC to run the code, as everything could simply be put onto the Raspberry pi. This drastically reduces the used space, whilst also increasing accuracy.

Finally, the most important aspect that can be improved/researched is detector geometry, so far, the only detector layout that has been tested is a square. This was done for its simplicity and ease of scalability. However, as can be seen in fig. 52, the detector accuracy depends greatly on the viewing angle of the sensor. Because of this, it is advised to research different shapes for a detector, an example could be a triangular detector, with SiPM's at each of the tips. Supposing the triangle is equilateral, the total viewing angle gets restricted to a mere 60 degrees, as opposed to the 90 degrees in fig 53. This should also offer the greatest accuracy-to-sensor ratio since it minimises the amount of sensors used (three) whilst also minimising the uncertainty.

The model is set up in such a way that it is easily expandable for different scenarios. Allowing one to, relatively easily, adjust or improve certain parameters. This allows for further research to be done without having to spend large sums of money on testing equipment.

7 Conclusion

During this five-month internship project, the groundwork has been laid for a fully-functioning muon tomography setup. Initially, it was looked at whether the proposed idea was feasible. This was done by first creating a robust model from scratch, that accurately describes the core physics at hand. From this it was clear that the proposed detector definitely has merit to become a fully functioning muograph.

After this, the model was verified with close agreement to the measurements, having an error of approximately 5% when measurements were taken at the centre of the scintillator. This close agreement gave confidence that the model is accurate, reinforcing the statement that the proposed idea can indeed become a proper muon tomography detector.

The dependence on detector geometry was also researched, showing that a 4 mm positional resolution is fairly easily attainable without an excessive sensor amount or a very thick scintillator. For small scintillators, a positional resolution of less than a millimetre could even be obtained given the amount of sensors is large enough. With improvements this accuracy could even be reduced with a more intelligent fitting algorithm, or other improvements that take into account more physical processes outside the scope of this report.

Lastly, a real-time muon detector was built by making use of in-house components at Nikhef. The setup of which was chosen following depth-length-sensor number graphs created using the model, these allowed a quick estimation of the expected positional resolution. Unfortunately, the estimated position resolution and the measured one differed by a factor two. However, this can be explained due to the fact that the electronics in the cosmic watch were simply not designed for such a task. In the future it would be better to create a custom circuit that handles data acquisition. It was found that placing the sensors at each face is unfavourable and instead it is recommended to place them at the corners. This allows for greater coverage over the entire detector.

This paper has shown that it is definitely possible to create an accurate muon detector using relatively inexpensive components. Using two of these detectors should already be enough to make a simple muograph. However, this will be left to a future project.

8 | Acknowledgements

9 | Literature

- [1] N Kume, H Miyadera, CL Morris, J Bacon, KN Borozdin, J Matthew Durham, K Fuzita, Elena Guardincerri, M Izumi, K Nakayama, et al. Muon trackers for imaging a nuclear reactor. *Journal of Instrumentation*, 11(09):P09008, 2016.
- [2] Donald E Groom and SR Klein. Passage of particles through matter. *The European Physical Journal C-Particles and Fields*, 15(1-4):163–173, 2000.
- [3] Sébastien Procureur, Kunihiro Morishima, and et al. Precise characterization of a corridor-shaped structure in Khufu’s Pyramid by observation of cosmic-ray muons. *Nature communications*, 14(1), 3 2023.
- [4] Jiang Hsieh. Computed tomography: principles, design, artifacts, and recent advances. 2003.
- [5] Valeri Tioukov, Andrey Alexandrov, Cristiano Bozza, Lucia Consiglio, Nicola D’Ambrosio, Giovanni De Lellis, Chiara De Sio, Flora Giudicepietro, Giovanni Macedonio, Seigo Miyamoto, et al. First muography of stromboli volcano. *Scientific reports*, 9(1):6695, 2019.
- [6] Edgar V Bugaev, A Misaki, Vadim A Naumov, TS Sinegovskaya, SI Sinegovsky, and N Takahashi. Atmospheric muon flux at sea level, underground, and underwater. *Physical Review D*, 58(5):054001, 1998.
- [7] Stephen L Lee, Ray Cywinski, and SH Kilcoyne. *Muon science: Muons in physics, chemistry and materials*, volume 51. CRC press, 1999.
- [8] Wikimedia Commons. Standard model of elementary particles, 2019.
- [9] CERN. The standard model, 6 2024.
- [10] Vitaliĭ Ginzburg. *The origin of cosmic rays*. Elsevier, 2013.
- [11] Mary K Gaillard, Paul D Grannis, and Frank J Sciulli. The standard model of particle physics. *Reviews of Modern Physics*, 71(2):S96, 1999.
- [12] Richard Phillips Feynman. Space-time approach to quantum electrodynamics. In *Quantum Electrodynamics*, pages 178–198. CRC Press, 1949.
- [13] Albert Einstein. On the electrodynamics of moving bodies. 1905.
- [14] NJ Rhodes. Scintillation detectors. *Neutron News*, 23(4):26–30, 2012.
- [15] Particle Data Group. Atomic and nuclear properties of materials for more than 350 materials.
- [16] Lev Davidovich Landau and Evgeni Mikhai lovich Lifshitz. *Course of theoretical physics*. Elsevier, 2013.
- [17] John Betteley Birks. Scintillations from organic crystals: specific fluorescence and relative response to different radiations. *Proceedings of the Physical Society. Section A*, 64(10):874, 1951.
- [18] J Drees and HE Montgomery. Muon scattering. *Annual Review of Nuclear and Particle Science*, 33(1):383–452, 1983.
- [19] Hans A Bethe. Moliere’s theory of multiple scattering. *Physical review*, 89(6):1256, 1953.

- [20] John E Sinko and Benjamin I Oh. The bouguer-lambert-beer absorption law and non-planar geometries. In *AIP Conference Proceedings*, volume 1402, pages 245–257. American Institute of Physics, 2011.
- [21] Sarah Eno and Matthieu Hamel. Organic scintillators-chap. 35.3. *The Review of Particle Physics/Reviews, tables & plots/Experimental methods and colliders/Particle detectors at accelerators*, pages pp–8, 2021.
- [22] William R Leo. Techniques for nuclear and particle physics experiments. *Nucl Instrum Methods Phys Res*, 834:290, 1988.
- [23] Onsemi. *Silicon Photomultipliers(SiPM), Low-Noise, Blue-Sensitive C-Series SiPM Sensors*, February 2022. Rev. 9.
- [24] S Cova, M Ghioni, A Lacaita, C. Samori, and F Zappa. Avalanche photodiodes and quenching circuits for single-photon detection. *Applied optics*, 35:1956–76, 04 1996.
- [25] Amelia Carolina Sparavigna. Poissonian distributions in physics: Counting electrons and photons. 2021.
- [26] CERN. Geant4, 2024.
- [27] Alberto Regadío, J. Ignacio García Tejedor, Sindulfo Ayuso, Óscar García Población, Juan José Blanco, Sebastián Sánchez-Prieto, and Óscar Rodríguez Polo. Trajectory determination of muons using scintillators and a novel self-organizational map. *Nuclear instruments and methods in physics research. Section A, Accelerators, spectrometers, detectors and associated equipment/Nuclear instruments & methods in physics research. Section A, Accelerators, spectrometers, detectors and associated equipment*, 973:164166, 9 2020.
- [28] SciPy 1.0 Contributors. curve fit — SciPy v1.14.0 Manual.
- [29] Spencer N Axani. The physics behind the cosmicwatch desktop muon detectors. *arXiv preprint arXiv:1908.00146*, 2019.

10 | Appendices

A. Scintillator as seen from a light source.

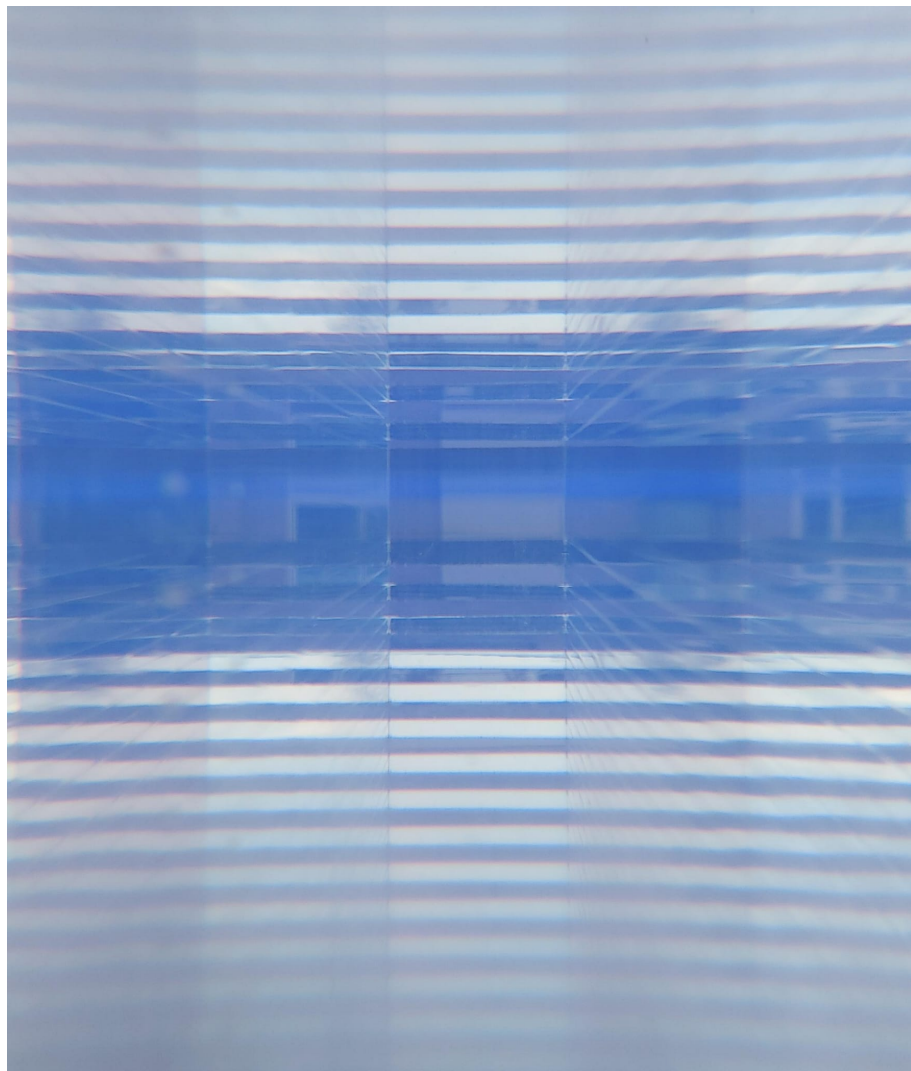


Figure 54: Scintillator seen from the perspective of a light source, the blueish tint comes from the scintillator reacting to UV light which starts scintillating. As can be seen, around the top and bottom, the frame gets increasingly more dim, this is due to the steeper angle the light makes, and therefore less light is measured.